Electrochimica Acta 469 (2023) 143246

Contents lists available at ScienceDirect

Electrochimica Acta

journal homepage: www.journals.elsevier.com/electrochimica-acta

Synthesis, characterization, functional testing and ageing analysis of bifunctional Zn-air battery GDEs, based on α-MnO_2 nanowires and Ni/NiO nanoparticle electrocatalysts

Yawar Salman [a], Sheharyar Waseem [a], Alessandro Alleva [a], Pritam Banerjee [b,c], Valentina Bonanni [d], Elisa Emanuele [a], Regina Ciancio [b,e], Alessandra Gianoncelli [d], George Kourousias [d], Andrea Li Bassi [a], Andrea Macrelli [a], Emanuele Marini [f], Piu Rajak [b,c], Benedetto Bozzini [a,*]

[a] Department of Energy, Politecnico di Milano, via Lambruschini 4, 20156, Milano, Italy
[b] Istituto Officina dei Materiali IOM-CNR, S.S, 14, km 163.5 in Area Science Park, 34149, Trieste-Basovizza, Italy
[c] Abdus Salam International Centre for Theoretical Physics, via Beirut 6, 34151, Trieste, Italy
[d] Elettra - Sinctrotrone Trieste S.C.p.A. S.S, 14, km 163.5 in Area Science Park, 34149 Trieste-Basovizza, Italy
[e] Area Science Park, Padriciano 99, Trieste, Italy
[f] Zentrum für Sonnenenergie- und Wasserstoff-Forschung Baden-Württemberg (ZSW), Helmholtzstraße 8, 89081, Ulm, Germany

ARTICLE INFO

KEYWORDS:
Zinc-air battery
Gas-diffusion electode
Oxygen reduction reaction
Oxygen evolution reaction
Microspectroscopy

ABSTRACT

Electrically rechargeable alkaline zinc air batteries (RZAB) – currently still at the R&D stage –, have great potential for stationary, as well as prospectively mobile, electrochemical energy storage applications. Their chief appeal is that they are made of abundant, environmentally friendly, intrinsically safe, and cheap materials, with established recycling concepts and auspicious life-cycle costs. One of the key weak points of present-generation RZAB programs is the air gas-diffusion electrode (GDE). In fact, on the one hand, GDE fabrication and testing are generally based on poorly understood protocols, and, on the other hand, performance is challenged by efficiency and durability issues. This work is centred on the fabrication of a novel bifunctional GDE for the air side of RZABs, on the assessment of its electrochemical performance and on the identification of factors impacting its efficiency and durability. The electrocatalysts for oxygen reduction reaction (ORR) and oxygen evolution reaction (OER) are α-MnO_2 nanowires and Ni/NiO nanoparticles, respectively. The composition of the active layer was optimized with rotating ring-disc electrode (RRDE) electrocatalysts tests. The GDEs were fabricated by spray-coating an ink, formulated with the electrocatalysts and the PTFE binder in an aqueous matrix. Fabrication and functional performance of GDEs – in pristine form and after ageing under realistic RZAB conditions – are rationalized on the basis of Scanning Electron Microscopy (SEM), Scanning Transmission X-ray SpectroMicroscopy (STXSM) at the Mn L-edge and Transmission Electron Microscopy (TEM) analyses. Imaging and spectral imaging disclosed the morphological and chemical-state evolution, brought about by electrochemical cycling. Special attention was devoted to the understanding of the role played by the presence of zincate in the electrolyte on the performance and ageing of the reversible air electrodes.

1. Introduction

The increasing demand of energy, expeditious economic growth and environmental issues, have prompted researchers and industries to explore new options in the domain of electrochemical energy storage (EES) solutions [1]. Lithium-ion batteries have been leading EES since the past few decades [2], but owing to issues like insufficient energy density (< 350 Wh/kg), high cost and safety risks [3], wide interest has been attracted by other EES options. Amongst them, zinc air batteries (ZABs) have demonstrated great potential owing to high theoretical energy density (1353 Wh kg^{-1}), lower manufacturing costs, availability of raw materials and inherent safety [4,5]. Specifically, an electrically

* Corresponding author.
E-mail address: benedetto.bozzini@polimi.it (B. Bozzini).

https://doi.org/10.1016/j.electacta.2023.143246
Received 25 March 2023; Received in revised form 20 August 2023; Accepted 21 September 2023
Available online 22 September 2023

rechargeable ZAB (RZAB) could be more advantageous than state-of-the-art Li-ion batteries for the stationary electricity storage, but, prospectively, also for heavy-duty mobility on road, rail and water.

An RZAB consists of a porous air cathode (gas diffusion electrode: GDE), a metallic Zn anode, and an appropriately ionically conductive alkaline electrolyte, usually immobilized in a polymer separator. During the discharge, the GDE supports the oxygen-reduction reaction (ORR), whereby oxygen impregnates through the porous substrate and is reduced on the electrocatalyst surface. During recharge, the oxygen-evolution reaction (OER) running at the GDE releases oxygen gas. Sluggish kinetics for both ORR and OER, limit the efficiency of the RZAB [6,7]. Corresponding high overpotentials at practically relevant current densities (c.d.s), especially in the anodic range (OER, charge), give rise to rapid degradation [8–10]. Thus, efficient bifunctional electrocatalysts which can support both OER and ORR at low overpotentials and sustain electrochemical cycling over a longer period are currently a hot research topic [11–13]. A crucial point for the optimization of oxygen electrocatalysis, is the accurate control of the GDE architecture, comprising a balanced combination of a hydrophobic and conductive substrate, onto which the electrocatalyst-containing active layer (AL) is coated. Ideal ALs should exhibit a high density of active and stable three-phase boundaries [14–16]. Specifically, the hydrophobized GDL ensures oxygen transport to the mildly hydrophilic catalyst layer (CL), simultaneously providing electronic contact. Hence, on the one hand, the development of active and stable electrocatalysts and, on the other hand, improvements in GDE fabrication - providing homogeneity of the active sites in the gas/electrolyte/catalyst triple-phase region - are simultaneously needed for practical rechargeable performance.

Various electrocatalysts have been investigated for RZABs, including Co_3O_4, $LaNiO_3$, AB_2O_4 spinels (A and B being divalent and trivalent ions respectively; A: Zn, Mn, Fe, Mg, Ni, Co and B: Mn, Cr, Co, Al, Fe), and Mn-oxides with different oxidation states, which show excellent catalytic performances [17–22]. MnO_2-based catalysts have recently gained much attention, owing to minimal cost, environmental friendliness and abundance, combined with low operational overvoltages [13,23-25]. By tuning the synthesis processes and parameters, a wide range of MnO_2 nanostructures can be obtained, with different electrochemical activity. In this work, we focus on α-MnO_2 which has recently emerged as a very prospective phase [26–29]. In particular, α-MnO_2 nanowires have been found to show stable ORR/OER cycling and high electrocatalytic activity [24,30,31]. Notwithstanding the mentioned reports on use of α-MnO_2 as bifunctional electrocatalist, it is worth noting that the present understanding of the underlying mechanisms is that use of a single material would be suboptimal. In fact, considering the generally recognized sequence of intermediate steps of ORR and OER processes, one can conclude that no single catalyst can optimize the reaction pathway in both directions (e.g. [32] and references therein). Thus, notable efforts are being devoted to the development of bifunctional electrodes based on mixtures of electrocatalysts individually optimized for ORR and OER [33–36]. Amongst dual-material bifunctional electrocatalysts, Mn-based transition metal oxides have been proposed for ORR [37,38] and nickel-oxides/hydroxides for OER [39–41]. Recent work explicitly addressed the combination of MnO_2 and Ni in GDEs for RZABs [42]. Specifically, in this work we proposed the fabrication protocol and a first-level description – based solely on electrochemical measurements – of the electrocatalytic impact of blending of α-MnO_2 and Ni/NiO nanoparticles (NPs). This pioneering work clearly showed the positive impact of this choice and opened up several fundamental issues regarding catalytic mechanisms and GDE formulation, but a systematic investigation of the AL composition and architecture, as well as molecular-level information on its behaviour are missing. Some of these issues have been tackled by our group through *in operando* XAS spectroelectrochemistry of full RZABs, for a particular AL composition [43,44].

The present work is aimed at a deeper and systematic understanding of the impact of catalyst composition and GDE fabrication of the electrochemical performance and ageing under realistic operating conditions, including electrochemical polarization sequences and exposure to Zn(II) in the electrolyte. The latter aspect has been recently pinpointed to have a crucial, often neglected, impact of MnO_2 performance [45]. Specifically, we have developed a highly reproducible protocol for: (i) α-MnO_2 synthesis; (ii) GDE formulation/fabrication and (iii) electrochemical GDE performance and durability testing. On the basis of this statistically qualified protocol, we have carried out a systematic study of bifunctional GDEs with α-MnO_2/Ni compositions in the range identified as promising in our preliminary work discussed in [42], solely on the basis of RRDE experiments. Finally, we have extensively characterized the morpho-chemical changes of the GDEs, brought about by ageing under controlled operating conditions. In particular, we adopted: (i) Scanning Electron Microscopy (SEM) to assess the morphology of whole GDEs; (ii) X-ray absorption microspectroscopy at the Mn L-edge to follow the chemical-state distribution and changes; (iii) Transmission Electron Microscopy (TEM) to verify the stability of the nanostructured electrocatalysts.

2. Materials and methods

2.1. Synthesis of α-MnO_2

α-MnO_2, the ORR electrocatalyst, was synthesized by a microwave assisted-hydrothermal method, with a protocol adapted from the literature [46]. 0.314 g K_2SO_4 (Sigma-Aldrich Chemie GmbH), 0.486 g $K_2S_2O_8$ (Sigma-Aldrich PTE Ltd.) and 0.203 g $MnSO_4{\cdot}H_2O$ (Merck, ACS, Reag. Pg Eur) were dissolved in 10 mL of Millipore water (Milli-Q® water, TKA, water conductivity 0.055 μS cm^{-1}). The solution was transferred to a 30 mL quartz reaction vial (G30 reaction vessel), equipped with a magnetic stirring bar, and then sealed. The mixture was held at 200 °C for 30 min in a microwave reactor (Monowave 400, Anton Paar GmbH), delivering the maximum power to keep the prefixed temperature. The stirring rate was set at 600 rpm. These conditions were empirically determined to ensure the formation of pure α-MnO_2, as assessed by XRD and Raman spectroscopy [45]. The collected mixture is centrifuged 5 times at 4350 rpm for 5 min. After each centrifugation step, the supernatant is extracted and replaced with Millipore water and shaken with a vortex mixer for 30 s. Since the synthesis process leads to the acidification of the aqueous matrix, the pH value of the liquid mix is controlled to check to effectiveness of the powder washing procedure. The washed synthesized product is dried overnight at 60 °C in a vacuum oven under a vacuum of ca. 100 mbar. Finally, the clumps resulting from the drying process are ground to a fine α-MnO_2 powder in an agate mortar.

2.2. GDE fabrication

The GDE formulation procedure for the preparation of the water-based electrocatalyst ink, employed PTFE as binder and hydrophobizing agent and carbon-black (CB) as conductivity promoter. After [47,48], the optimal PTFE content lies in the range 20÷30%. The PTFE/C-B/electrocatalyst ink is spray-coated onto C-paper [49]. Details of the GDE fabrication routes for different purposes are provided below. Details of the electrocatalyst compositions used for electrochemical tests are reported in Tables 1 and 2.

It is worth noting that – in addition to its scientific and technological merits – our GDE fabrication protocol, also compares favourably with existing ones in terms of cost-effectiveness, from two different aspects: electrocatalyst synthesis and coating technique.

As far as electrocatalyst synthesis is concerned, in the context of synthesizing α-MnO_2 (cryptomelane), our chosen method, the microwave-assisted technique, presents significant benefits for small-scale production, most notably its speed. The process reaches completion in only 10 min, while the conventional hydrothermal technique typically spans 12–48 h [50,51]. The microwave-assisted technique is

Table 1
Compositions of electrocatalyst inks produced for active layers tested in RDE/RRDE measurements.

Ink type	Ni/NiO [mg]	C [mg]	α-MnO2 [mg]	Nafion Solution [mL]
Carbon black (CB)	0	16	0	4.0
α-MnO_2	0	0	16	4.0
0 wt% Ni/NiO	0	8.00	8.00	4.0
10 wt% Ni/NiO	1.6	7.20	7.20	4.0
23 wt% Ni/NiO	5.33	5.33	5.33	4.0
50 wt% Ni/NiO	8.00	4.00	4.00	4.0

particularly valuable during preliminary studies, prototyping phases, or when frequent iterative modifications are essential, establishing its cost-effectiveness. On the other hand, when the focus is scaling-up for industrial mass production, conventional hydrothermal synthesis becomes more viable, owing to its capacity for larger batches and its widespread acceptance in industry. It is noteworthy that continuous flow microwave reactors are being explored for potential industrial applications. However, the initial capital investment for such microwave systems, given their complexity, is expected to surpass that of conventional hydrothermal methods, which are already commonly available and well established.

Regarding the coating technique, spray coating is the method of choice in small-scale studies for gas-diffusion electrode preparation. It allows precise control over active material loading; each spray directly correlates to the weight of the deposited material, enabling meticulous adjustments during development. Additionally, spray coating facilitates rapid iterations, making it cost-effective for experimental phases. However, spray coating adaptability is constrained during large-scale production. For such applications, doctor blading becomes preferable. It consistently produces uniform films over large areas, especially once an optimal electrode composition is established [52].

2.2.1. Monofunctional catalyst ink

Inks for ORR GDEs were prepared by dissolving 40 wt% CB nanopowder (C—NERGY SUPER C65, Imerys Graphite & Carbon), 40 wt% α-MnO_2 (in-house synthesized) and 20 wt% PTFE (59 wt%, 3M™ Dyneon™ PTFE TF 5060GZ) in 16.2 mL of deionized water. The mixture was first agitated with a magnetic stirred for 10 min and then sonicated for 1 min at 10 W with a tip sonicator (UP200St, Ultrasonic processor, Hielscher Ultrasonics GmbH) to achieve optimal nanowire dispersion. Subsequently, the mixture was homogenized (PT2500E Polytron, Kinematica GmbH. Tip type: PT-DA 12 / 2EC-E157) at 30,000 rpm for 1 min.

2.2.2. Bifunctional catalyst ink

Inks for ORR/OER GDEs were fabricated by mechanically mixing α-MnO_2 nanowires and Ni/NiO NPs (APS 5–20 nm, 99.9% (metals basis), Alfa Aesar). Three different bifunctional ink compositions were prepared following the same fabrication protocol as for the monofunctional ink. The three compositions were defined with the following proportions, referring to solid wt%: $(C)_A(\alpha\text{-}MnO_2)_A(Ni/NiO)_B(PTFE)_{100-2A-B}$. (i) $A = 32.5\%$, $B = 10\%$, (ii) $A = B = 23\%$, (iii) $A = 12.5\%$, $B = 50\%$. These compositions were selected because they sample, with a reasonable step, the optimal range identified in previous work in our group, allowing to refine the identification of the best proportion of ORR and OER dedicated electrocatalysts. Specifically the intermediate Ni/NiO NP contents (10% and 23%) span the optimal bifunctional catalyst composition considered in our preliminary work, while the extreme values (0% and 50%) allow to pinpoint the bifunctional behaviour of ALs in which the with purely ORR electrocatalyst (0%) with a high proportion of OER electrocatalyst (50%), that makes the amount of the ORR surely suboptimal. It is worth noting here, that ink formulation tests revealed, empirically, but quite evidently, hydrophilic behaviour of Ni/NiO NPs. Specifically, we did not notice any appreciable agglomeration phenomenon, suggesting that the particles exhibit affinity towards water. Furthermore, surface wettability tests of nikel oxide films and nanoparticles for supercapacitor applications [53, 54] have positively proved that NiO exhibits hydrophilic behaviour, with contact angles significantly below 90°.

2.2.3. Spray-coating on C-paper support

Hydrophobized carbon paper with 60wt% of PTFE (Fuel Cell Store: Toray Paper 090-TGP-H-090 60wt%, 40 cm × 40 cm) was cut into 9 cm × 3 cm stripes. The Toray-paper support was fixed on the hot-plate of the spray-coating system. Spraying was performed with a Badger Air-Brush (Co. 350 Mobile Tech Airbrush), fed with N_2 at 4 bar. The spray-coating procedure was optimized and consolidated with scrupulous replication to achieve an operator-independent narrow distribution of electrochemical performances (for details, see Section 2.3). The salient details are provided below: (i) batches of 20 mL of ink were processed directly in the dispenser jar of the airbrush and kept under magnetic stirring at 900 rpm, till the moment of use; (ii) after each deposition run, the airbrush was totally dismounted and all components were thoroughly cleaned with isopropyl alcohol; (iii) the settings of the nozzle and nozzle-sample distance (18 ± 0.5 cm) are calibrated with specifically developed references; (iv) the sweep rate (7 ± 10% cm s^{-1}) and the sequence and pattern of strokes (combination of alternating vertical and horizontal stokes, in clockwise rotation) were accurately defined. The sweep rate, waiting time between strokes and hot-plate temperature (65 ± 0.1 °C), were optimized to avoid cracking and to ensure morphological homogeneity down to micrometre scale, as assessed by SEM (field emission scanning electron microscope (FE-SEM) Zeiss SUPRA 40). After spray coating, the GDE was heat-treated at 330 °C for 30 min in a retort oven under N_2 flux, to optimize PTFE distribution. The weight-gain of the GDE was finally evaluated, to estimate the catalyst loading.

2.3. Electrochemical testing

2.3.1. Half-cell setup for GDE testing

As-fabricated GDE stripes were cut in two portions and mounted in a commercial half-cell setup (Gaskatel GmbH, Flex cell), with a Pt

Table 2
List of GDEs studied in this work, with indication of electrocatalyst composition, loading and type of electrochemical test to which they have been subjected. In this work, electrocatalyst compositions will be indicated as follows. A: 0 wt% Ni/NiO; B: 23 wt% Ni/NiO, C: 10 wt% Ni/NiO and D: 50 wt% Ni/NiO.

GDE	C : MnO_2 : Ni/NiO ratio in AL [wt%]	Catalyst to PTFE ratio in [wt%]	Loading L [mg/cm^2]		Electrochemical conditions
Series A -Galvanostatic Staircase	40 : 40 : 0	80 : 20	A_1	0.52	ORR
			A_2	0.58	
			A_3	3.01	
			A_4	4.35	
			A_5	5.17	
			A_{10}	5.06	
Series A – RSP (A_6, A_7, A_8, A_9)	40 : 40 : 0	80 : 20	4.99 ± 0.625		ORR/OER
Series B – RSP (B_1, B_2, B_3)	32.5 : 32.5 : 10	75 : 25	5.42 ± 0.223		ORR/OER
Series C – RSP (C_1, C_2, C_3)	23.3 : 23.3 : 23.3	70 : 30	5.67 ± 0.196		ORR/OER
Series D – RSP (D_1, D_2, D_3, D_4)	12.5 : 12.5 : 50	75 : 25	5.25 ± 0.464		ORR/OER

counter-electrode, modified with an Hg/HgO reference electrode. The active area of the air electrode was 3 cm^2. The electrolyte compartment of the cell was filled with 30 mL of 6 M KOH solution, without or with addition of 0.1 M ZnO, as specified where relevant. All the measurements were performed under oxygen flux (7 nlt h^{-1}) at ambient temperature.

2.3.2. Rotating-Disk Electrode (RDE)/rotating ring-disk electrode (RRDE) setup

The electrocatalytic activity and stability of ORR electrocatalysts were evaluated using a rotating ring-disk electrode (RRDE) setup (Pine Research Instrumentation, based on an MSR Rotator), driven with a rotational speed controller (Model AFMSRCE, Pine Instrument Co.), coupled with a bipotentiostat (VMP-300, biologic Science Instruments). The same configuration was also used without electrode rotation, since this type of mass-transport control is not required for a gas-evolving electrode, for OER electrocatalysis tests. A typical three-electrode system was employed, including a catalyst-coated glassy carbon electrode with Pt ring (GC, Diameter 5 mm, Pine research Instrumentation) as the working electrode, a platinum wire (AMEL), as the counter electrode, and Hg/HgO electrode in 0.1 M KOH solution as a reference electrode. The working electrode was polished before each measurement with a 0.3 μm alumina slurry on microcloth, washed with acetone and then dried. The Pt ring was cleaned with acetone on a cotton paper after each test.

2.3.2.1. Drop-cast glassy-carbon, electrodes. To carry out the analytical tests, electrodes were prepared by drop-casting the active material onto a glassy carbon substrate (glassy carbon disk inserts, Pine Research Instrumentation). For each of the different ink formulations, a drop-casting solution was prepared in the following way: first, a Nafion solution was prepared by mixing 39.85 mL of Milli-Q water, 10.00 mL of ethanol (EtOH, Sigma-Aldrich) and 0.350 mL 5 wt.% Nafion™ 117 solution (Sigma-Aldrich). The solution was kept under magnetic stirring till it is used. Then, a total of 16 mg of material was magnetically stirred for 10 min and then sonicated for 1 min at 10 W, in 4 mL of the aforementioned Nafion solution. The so-obtained ink was kept under stirring for a minimum of 12 h and then drop-cast onto the glassy carbon electrode. The electrode was then left to dry at room temperature while rotating at 500–600 rpms.

2.3.2.2. ORR electrocatalysis experiments. were carried out with the following protocol: electrolyte aliquots of 150 mL, hosted in a dedicated cell for RRDE/RDE, closed to exchange with ambient air, were outgassed with N_2 bubbling for at least 20 min and 10 cyclic voltammetry (CV) cycles were measured in the range $-0.8 \div 0.3$ $V_{Hg/HgO}$ at 5 mV s^{-1}. Then, the solution was saturated with O_2 for at least 20 min and the same CV measurements were repeated. The linear sweep voltammograms (LSV) were determined in an O_2-saturated 0.1 M KOH solution (Merck, Titripur®, Reag. Ph Eur), stepping the electrode rotation rate at the following values: 0, 500, 700, 1000, 1200 and 1600 rpm. The potential of the disk electrode was swept from -0.8 $V_{Hg/HgO}$ to $+0.1$ $V_{Hg/HgO}$ and the potential of the ring electrode was set at $+0.5$ $V_{Hg/HgO}$. Three independent replicates of each LSV was measured, to ensure statistical robustness. In order to assess potential loss of material from the electrocatalytic film - resulting in a reduction of surface area and catalyst activity - measurements at 1600 rpm were repeated three times for each sample: one at the beginning of the test, one after having performed half of the LSV scans at different rotation rates and one at the end of the whole experiment. Finally, N_2 was bubbled for 20 min, thus allowing to repeat the measurement of the c.d. profile in the absence of ORR. This served as the blank measurement and was then subtracted from the other profiles during the evaluation of the data. Data-processing details are reported in Section S1 of the Supporting Information. Capacitance effects have been accounted for in the LSV scans and quantitative analyses have been carried out with the tangent method.

2.3.2.3. OER electrocatalysis experiments. were carried out with the same set-up used for the ORR study, using the ring disk electrode without rotation. LSVs were performed at 5 mV s^{-1} in 0.1 M KOH in the potential range $0.6 \div 1.0$ $V_{Hg/HgO}$. Capacitance effects have been accounted for in the analysis of the LSV curves.

2.4. TEM microscopy and HAADF-STEM experiments

Specimens suitable for TEM studies were prepared by drop-casting onto Au TEM grids a suspension of the AL material, extracted from a given GDE. The suspension was prepared by scraping off the AL of the GDE from the carbon paper support, adding isopropanol (with isopropanol / AL chips proportion of 3 mL / 1 mg) and then sonicating the mixture using a tip ultra-sonicator at 10 W for a one min. TEM and high-angle annular dark-field (HAADF) scanning TEM (STEM) experiments were performed using a JEOL 2010 UHR field emission gun microscope, operated at 200 kV with a determined spherical aberration coefficient *Cs* of 0.47 ± 0.01 mm. HAADF STEM images were obtained using an illumination angle of 12 mrad and a collection angle of $88 \leq 2\theta \leq 234$ mrad. The nanostructural analyses were complemented with Energy Dispersive X-ray Spectroscopy (EDS), using a Oxford (Silicon Drift Detector) with a 80 mm^2 active window.

2.5. Scanning transmission X-ray spectromicroscopy (STXSM)

The samples for STXSM were prepared in the same way as these for HRTEM, but using an isopropanol / AL chips proportion of 0.5 mL / 1 mg. STXSM at Mn L-edge was conducted at TwinMic beamline of Elettra Trieste synchrotron facility. In scanning transmission X-ray microscopy, a diffractive focusing lens forms a microprobe on the sample plane, while the specimen is raster-scanned across it on a pixel-by-pixel base. A fast-readout CCD camera collects the X-ray photons transmitted by the sample point by point in the raster scan, producing absorption and differential phase contrast images [55]. For the present experiment, stacks of images were acquired across the Mn L-edges (638.7 and 649 eV). To jointly optimized energy resolution in the ranges that are crucial for chemical-state assessment, and experimental time, a step of 1 eV was chosen: (i) in the pre-edge range from 634 to 636 eV, (ii) in the range between-edges 642–647 eV and (iii) in the post-edges zone from 652 to 656 eV. The range around the first edge from 636 to 642 eV was scanned with higher resolution in steps of 0.25 eV, while in the less diagnostic range 647–652 eV the energy step was set to 0.5 eV. At each energy step, the zone-plate based diffractive optics was automatically refocused on the samples, delivering a probe size of around 250 nm in diameter. The samples were mounted on Au TEM grids covered with formvar film to ensure suitable transmission in the desired energy range. Appropriate post-processing and alignment of the collected stack of images enabled the extraction of XAS spectra on a pixel-by-pixel base.

3. Results and discussion

Our experimental study of GDEs, fabricated as described in Sections 2.1 and 2.2, is centred on the combination of electrochemical testing, microscopy, structural analyses by TEM and chemical-state sensitive spectromicroscopy. GDEs in pristine and electrochemically aged conditions are compared in view of rationalizing the factors favouring electrocatalytical activity and durability, and to pinpoint the degradation processes.

Electrocatalytic tests on the active materials and on complete GDEs are reported in Sections 3.1 and 3.2. SEM and HRTEM imaging is described in Sections 3.3.1 and 3.3.2, respectively. Structural analyses are reported in Section 3.3.2 and X-ray absorption spectromicroscopy results are presented in Section 3.3.3.

3.1. ORR and OER electrocatalytic activity evaluation (RRDE voltammetry analysis)

Bifunctional GDEs must be highly active for both ORR and OER reactions and remain stable over time. In this Section, we report a systematic study on the influence of ink composition on the cathodic and anodic oxygen reactions.

To test the catalytic performance of the ORR, the protocol described in Section 2.3.2. was used. In order to obtain electrocatalytic results that are fully representative of the material under operating conditions, it is important to apply an electrochemical conditioning treatment, prior to RRDE tests. This is crucial to discriminate – as we have recently pinpointed in [45] and it will become clearer from our XANES results of Section 3.3.3 – the real electrocatalytic response from the evolution of pristine MnO_2. Further details are provided in Section S2 of the Supporting Information.

A systematic investigation of the rotation-rate dependant RDE LSVs for the ORR performance has been performed and the results are reported in Figure S2 and commented in Section S3 in the Supporting Information. These data have been elaborated with the Koutecký–Levich method, as detailed in Section S1 and Table S1 of the Supporting Information. The ORR RRDE disk-c.d. curves are reported in Fig. 1(a), and the mechanistic parameters - extracted from them with Eqs. (S4) and (S5) of Section S1 of the Supporting Information - are shown in Fig. 1(b).

The number of electrons obtained from the RRDE measurements and the fraction of HO_2^- produced, are reported in Fig. 1(b), and indicate a four-electron oxygen reduction mechanism. The peroxide production, resulting from incomplete O_2 reduction, was low and hardly dependant on the electrode potential and CB fraction.

In addition to ORR mechanism assignment, the LSVs of Figure S2 yield additional information regarding electrocatalytic activity, on the basis of the onset potential, which can be conveniently determined by measuring the overpotential at the kinetic c.d. of 1 mA cm^{-2}, as detailed in the Section S4 of the Supporting Information. The onset potentials of the investigated materials were found to rank as follows: α-MnO_2 (−0.12 V) > 50% Ni (−0.05 V) > 10% Ni (−0.03 V) > 23% Ni (−0.003 V) > 0% Ni (−0.00 V). Since addition of Ni/NiO NPs is meant to enhance OER activity (see next paragraph), its role towards ORR performance is just to dilute the ORR-active α-MnO_2, catalyst. Hence the result that the higher the amount of Ni/NiO NPs, the lower the limiting c.d. and the more negative the onset potential. The addition of CB in the ink clearly enhances the ORR activity of α-MnO_2. Morever, use of CB as catalyst support indeed improves electrical conductivity, but – in addition – the volcano-shape behaviour highlighted in our preliminary investigation described in [42] - with the lowest overpotential found at $(C)_{50}(MnO_2)_{50}$ -, suggests that surface concentration plays an important role in ORR. In particular, this findig hints at the fact that the MnO_2-C contact might have a specific electrocatalytic effect: this point has been addressed spectroscopically in Section 3.3.3.

As far as OER is concerned, quite predictably, LSVs show that the electrocatalyst with 50% Ni presents the highest activity (Fig. 1(c)). As far as the Ni-free electrocatalyst is concerned, we found a sizable

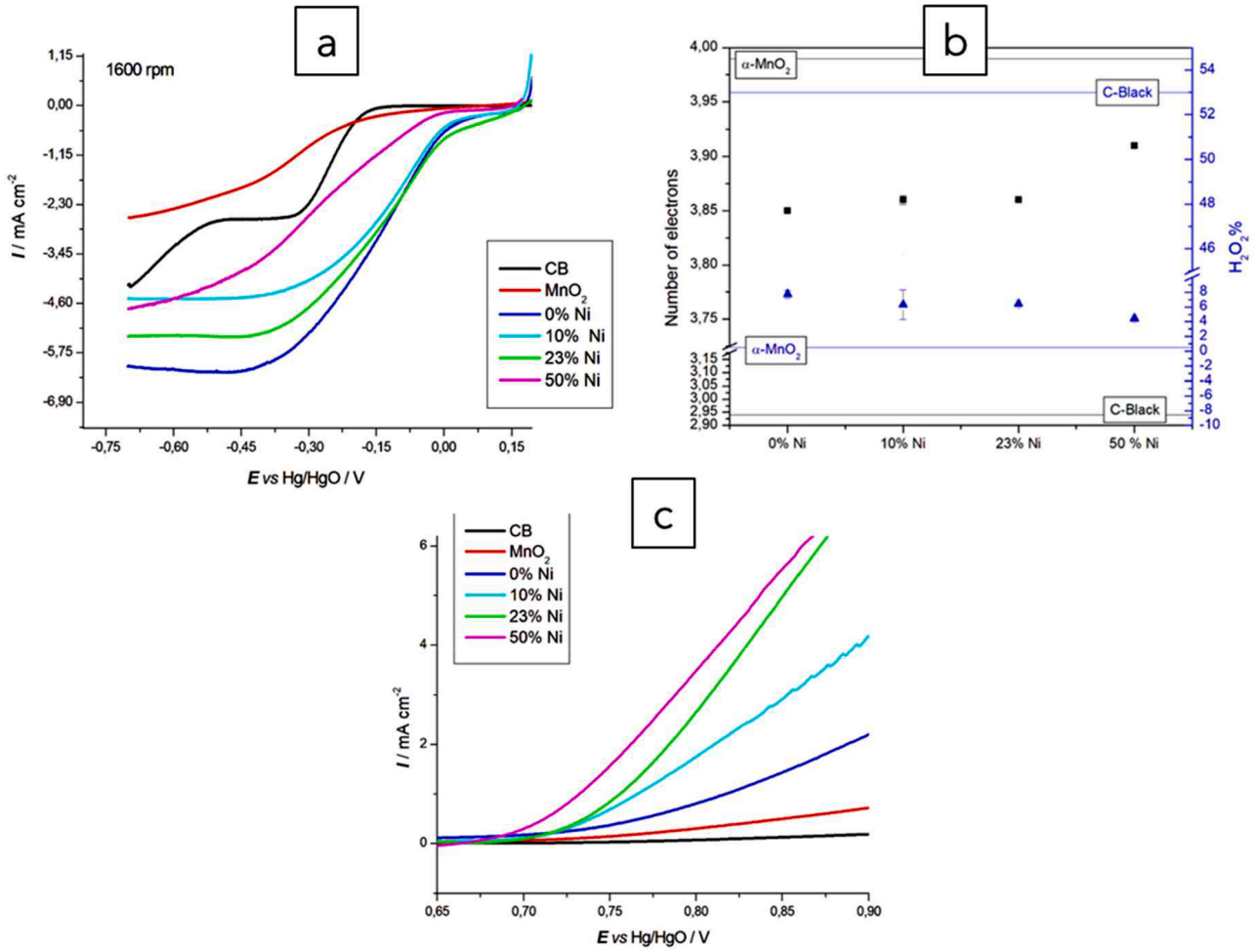

Fig. 1. (a) RRDE LSVs (disk current density) RRDE ORR electrocatalytic tests, run at 1600 rpm, for the indicated materials. For details, see Sections 2.3.2.2 and 3.1. (b) ORR mechanism parameters derived from RRDE measurements for the indicated electrocatalysts. For details, see Section S1. (c) LSVs for OER electrocatalytic tests of the indicated materials. For details, see Sections 2.3.2.3 and 3.1.

improvement of the OER activity – though, much lower than that brought about by Ni/NiO NP additions – if CB is added to pure α-MnO_2, in keeping with the reported high OER activity of manganese oxide/carbon heterostructures [56–59]. In fact, these literature studies report that a good MnO_x OER catalyst should exhibit two different features: (i) Mn ions connected by a flexible network of μ-oxido ligands within a less structured oxide, enabling substrate attachment and turnover, and this is the case of α-MnO_2 adopted in this work, and (ii) the stabilization of Mn^{3+}ions to be available for oxidation state changes at OER potentials. A third aspect, that has not been explicitly addressed in the literature, is that during ORR reactions, new active sites at MnO_2-C boundaries can be created, that result in a higher OER activity. The second and third aspect have been addressed spectroscopically in Section 3.3.3 below. Morever, CB can counteract the low conductivity of Mn oxides, improving OER activity as a result of lower ohmic drops. Moreover, in the presence of Ni/NiO NPs, the activity increases upon bringing the CB fraction from 10 to 23 wt%. The electrocatalyst containing 10% of Ni/NiO NPs exhibits the worst activity, probably because the C% reaches the suboptimal value of 45%.

3.2. Electrochemical testing of ORR/OER bifunctional GDEs

Even though ORR and OER electrocatalysts *per se* can be tested and – at least, in part – understood mechanistically on the basis of electrochemical tests of the type described in Section 3.1, nevertheless, the same electrocatalyst, once incorporated into a GDE can yield a variety of performances, as a result of the details of AL composition and architecture. In fact, the complex GDE formulation process adds sources of variance that cannot be easily quantified and rationalized. Moreover, as far as durability is concerned, a range of GDE degradation mechanism can impact the device operation even in the absence of electrocatalyst deterioration. Literature studies aimed at enhancement of durability, have mainly concentrated on contrasting electrolyte leakage through the GDE [43,60-61], minimizing clogging by electrolyte carbonation from atmospheric CO_2 [62–66] and following the deterioration of the PTFE-based binder [4], but limited information is available on the actual evolution of the AL composition and architecture.

For electrochemical testing, the GDEs fabricated as described in Section 2.2 and listed in Table 2, were employed as working electrodes in the half-cell setup described in Section 2.3.1, and tested with different electrochemical procedures for ORR and bifunctional operation. These testing protocols are explained in this Section and in Section S4 of the Supporting Information. The electrolyte employed was 6 M KOH, typical of ZABs, without and with added 0.1 M ZnO, simulating the buildup of anodic dissolution products. In particular, in view of methodology development and for reference, we have first carried out a thorough investigation of the monofunctional ORR electrodes (Section S4 of the Supporting Information), and then proceeded to the systematic testing of ORR/OER bifunctional electrodes (this Section).

It is well known that air electrodes are critical components in RZABs, owing to typically high OER overvoltages and faster failure brought about by the highly oxidizing polarization imposed during charging, impacting both the electrocatalyst and the electrocatalyst support [23,67,68]. As hinted at in the Introduction, amongst many possible ways of attacking this combined activity and durability issues, we resorted to the bifunctional approach, centred on the combination of dedicated electrocatalysts for ORR and OER. Specifically, we employed α-MnO_2 nanowires for ORR and Ni/NiO NPs for OER. Ni is an excellent OER catalyst and the potential it imposes results in protection of the carbon-based electrocatalyst support that would tend to oxidize at the anodic potentials needed to run OER with α-MnO_2 [69,70]. This effect is indeed confirmed, but it is worth noting thar, when used in conjunction with ORR catalyst, Ni/NiO NPs exhibit complex synergies that still need to be fully understood [24,42].

In this study, we developed and applied a rapid screening protocol for the efficient and reliable testing of bifunctional air electrodes. This test consists in repeating three sequences of cathodic/anodic galvanostatic steps, with intervening Electrochemical Impedance Spectrometry (EIS) measurements. The cathodic c.d. was selected on the basis of the indication that, in view of developing a commercially viable RZAB system, they must have capacity of more than 11.7 mAh cm^{-2} [71]. Keeping this value as a reference point, we set anodic and cathodic c.d.s and the corresponding holding times yielding an areal capacity of 20 mAh cm^{-2}, that would correspond to a highly competitive performance. With this guideline, we fixed a constant, rather aggressive discharge c.d. of 60 mA cm^{-2} and a sequence of charging c.d.s ranging from 10 to 90 mA cm^{-2}: the lower limit corresponds to a classical recharge rate and the upper one to very aggressive fast-charging conditions. In order to obtain a better grasp on the evolution of the electrode performance, galvanostatic EIS measurements under applied cathodic bias were carried out at the end of the ORR intervals at the discharge c.d.. EIS spectra were recorded in the frequency range from 200 kHz to 100 mHz with a c.d. modulation of 5 mA cm^{-2}. The cathodic behaviour was selected for EIS tests, because this process is more diagnostic of the details of electrocatalyst stability, as well as AL structure and hydrophobicity. With these settings, a test can be completed in 24 h. More details of the test protocol are provided in Figure S6 of the Supporting Information. The rationale of the sequence of applied OER c.d.s in each of the three test periods is that of imposing relatively mild, but practically relevant recharge conditions (10 mA cm^{-2}) for one third of the period, successively switching to aggressive ones (30 and 60 mA cm^{-2}), alternated with a period of stress conditions (90 mA cm^{-2}). Similar – though quantitatively different – testing concepts are documented in the literature [24].

3.2.1. Testing of bifunctional electrodes in zincate-free 6 M KOH electrolyte

The bifunctional electrodes with the C/α-MnO_2/(Ni/NiO) NP proportions discussed in Section 2.2.2 and summarized in Table 2, were tested with the rapid screening protocol of Figure S6 of the Supporting Information, first in a pure KOH electrolyte (present Subsection) and then with added 0.1 M ZnO (SubSection 3.2.2).

Fig. 2 reports the results of the bifunctional testing for GDEs without Ni/NiO NPs (GDE A) and with the following Ni/NiO NPs amounts: 10 (GDE B), 23 (GDE C), 50 wt% (GDE D). The left Subpanels of each Panel show the mean potential profiles and the corresponding standard deviation bands, estimated from five to seven independent replicated experiments. The right Subpanels display representative series of EIS spectra in Nyquist plot form. Figure S7 of the Supporting Information reports all the replicates of the measured potential time-series.

The potential time-series for GDEs without Ni/NiO NPs (GDE A) in Fig. 2, shows that the response remains steady in the initial cycle and in the two low-c.d. intervals of the second cycle, after which the polarization starts to increase. Oxidation of the electrocatalyst support, brought about by the high anodic potential in the OER periods, is the main reason of this progressively increasing polarization. It is worth noting that, even in the absence of a dedicated OER catalyst, the GDEs performed well, with adequate overpotentials, in the first two cycles: this is coherent with literature results regarding the electrocatalytic performance of pure α-MnO_2 towards OER [69,70]. In matching with the potential time-series, the sequence of EIS Nyquist plots of GDE A shows that, concomitantly, the mass-transport resistance starts to increase after the completion of the second cycle, while the charge transfer resistance is essentially constant. It is worth noting that the EIS spectra evidence, even more clearly, the training effect of the electrocatalyst, showing that the charge-transfer and the ohmic resistances decrease over the few GS steps. This behaviour correlates with loss of hydrophobization, accompanied by AL cracking, as the key GDE damaging mode, and corrosion of conductivity carbon can be the process triggering these phenomena. These results provide a factual basis for the strategy of decreasing the OER overvoltage with a dedicated electrocatalyst – Ni/NiO NPs in this case – in view of improving the durability of bifunctional GDEs.

The same accelerated ageing test was thus repeated for GDEs

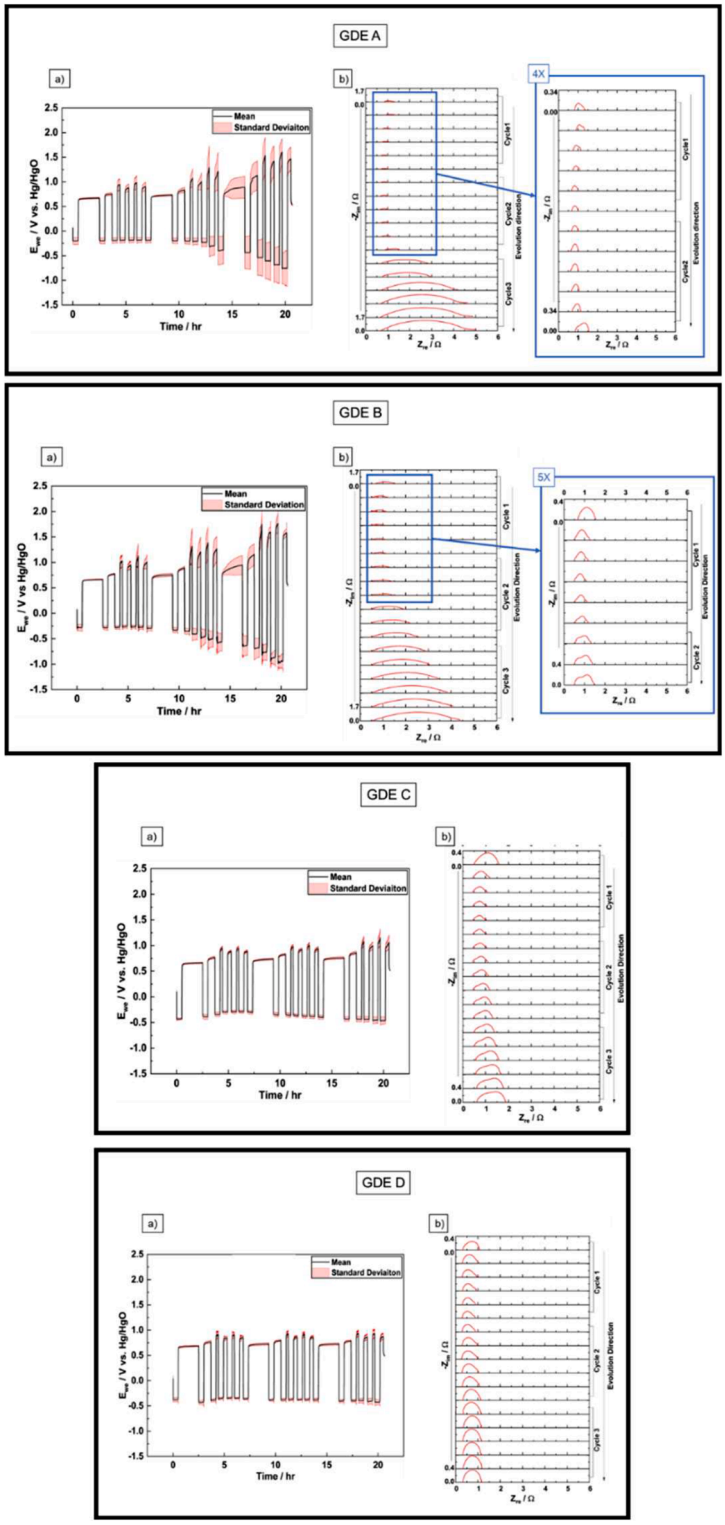

Fig. 2. Results of the OER/ORR rapid screening protocol (see Section 3.2.1 and Figure S7 of the Supporting Information) for replicates of GDEs with different fractions of Ni/NiO NPs. GDE A: 0 wt%; GDE B: 10 wt%; GDE C: 23 wt%; GDE D: 50 wt%. The left Subpanels of each Panel report the means and standard deviations of the potentials, and the right Subpanels, the galvanostatic EIS results (Nyquist plots) measured with −60 mA cm^{-2} bias.

fabricated with the Ni/NiO NPs fractions of Table 2, with the aim of identifying the optimal composition.

The results of Fig. 2, referring to GDE B with 10 wt% of Ni/NiO NPs, show that the anodic overvoltages are larger than in the GDEs without Ni/NiO NPs, and that the overvoltage increase starts from the higher c.d. s of the first cycle. The behaviour of the ORR branch is, instead, essentially the same for GDEs without and with 10 wt% Ni/NiO NPs. Like in the case of GDE A, the EIS spectral patterns of GDE B start to change in correspondence of the attainment of the c.d. level giving rise to a drastic increase of anodic overvoltage (60 mA cm^{-2} on the first cycle). The charge-transfer and mass-transport resistances exhibit the same behaviour observed in the absence of Ni/NiO NPs, but the ohmic

resistance is more stable in the presence of 10 wt% Ni/NiO NPs. The electrocatalyst training effect can be observed from the first EIS spectra also with this bifunctional GDE. From the comparison of GDEs without and with 10 wt% Ni/NiO NPs, it can be concluded that the metal content somehow increases the electronic conductivity of the AL, but the beneficial effect of the added OER electrocatalyst has not fully developed. Moreover, the added solid load seems to unbalance the AL structure towards a less performing form, possibly owing to the hydrophilic nature of Ni/NiO NPs.

In the GDEs with 23 wt% of Ni/NiO NPs (GDE C), it is evident that the OER overvoltages are notably lower, and stable, over all the three test cycles: in correspondence the ORR overvoltages are stable, but slightly higher than with GDEs A and B. With this particular Ni/NiO NPs loading, the desired effect on both OER and ORR can be attained, though at the cost of a slight overvoltage increase in the ORR branch – possibly due to the smaller loading of ORR-active α-MnO_2 and the increased hydrophilicity – effectively counterbalanced by an improvement in cycling stability. This confirms that lower anodic overvoltages improve the stability of the ORR performance. The EIS data of GDEs C show that changes in spectral pattern can be noticed only starting with the third cycle, and are essentially due to an increase by a factor of two of the mass-transport resistance. This result confirms that GDE degradation is controlled by progressive flooding of the gas channels. Coherently with the increase of metal content, the ohmic resistance is slightly lower than that found with 10 wt% Ni/NiO NPs. Moreover, the electrocatalyst training effect is faster in this case, and it is essentially completed within the first two GS steps. This behaviour suggests that the presence anodic potential control, afforded by Ni, stabilizes the valence state of Mn(III). This point will be explicitly addressed by XANES results of Section 3.3.3.

Lastly, we evaluated the performance of GDEs with 50 wt% Ni/NiO NPs (GDEs D). Overall, the effect of increasing the Ni/NiO NP content from 23 to 50 wt% is limited, suggesting that Ni addition exhibits a sort of threshold behaviour, in the composition range investigated. A closer look at the potential time-series reveals that the trends in the changes of ORR and OER performances found with 23 wt% Ni/NiO NPs are confirmed also with 50 wt%. In fact, the OER performance is slightly improved, both in terms of overvoltage and stability over cycling. In correspondence, slightly higher, though very stable, ORR overvoltages were recorded. EIS spectra exhibit very limited changes in spectral pattern, that can be explained with a slight increase of the mass-transport resistance. This behaviour of the EIS spectra further witnesses the remarkable stability of the GDEs formulated with this composition.

A synthetic comparative view of the impact of the Ni/NiO NPs content of the GDE performance data of Fig. 2 can be gained by considering the mean values of the potential time-series (summarized in Figure S8(a)) and the progressive change in series resistance, as estimated from the EIS spectra (summarized in Figure S8(b)). A clear threshold effect can be appreciated for the Ni/NiO NP content: 23 wt% allowing a significant and stable decrease of the OER overvoltage, accompanied by a stabilization of the ORR response. This stabilizing effect is further emphasized by the fact that the standard deviations, plotted in Fig. 2, decrease with increasing Ni/NiO NPs fraction. For short testing times, before the expression of the stabilizing action, adding Ni/NiO NPs brings about an increase of the ORR overvoltage: coherently with the results of Section 3.1: this can be explained with the lower α-MnO_2 loading. Nevertheless, this partial loss of ORR performance is largely compensated for by the stabilization of the ORR branch of the test cycle.

3.2.2. ORR/OER testing of electrodes in the presence of Zn(II)

To assess the impact of the presence of zincates on the performance of GDEs under realistic operating conditions, the rapid-screening tests described in Section 3.2.1 were repeated in 6 M KOH + 0.1 M ZnO electrolytes for the GDE with the optimal Ni/NiO NPs loading of 23 wt% and, for reference, without the OER electrocatalyst.

Fig. 3 shows that, for the GDE without Ni/NiO NPs (GDE A), both ORR and OER overvoltages are notably higher in the presence of zincates. Moreover, in the latter case, the test is terminated during the second cycle, because the OER cutoff is reached. In the ORR branch, the performance in the presence of zincates is clearly worse right from the beginning of the experiment, and it degenerates when the anodic step at 60 mA cm^{-2} of the second cycle is reached. In the OER branch, the overpotential diverges at 40 mA cm^{-2} in the first cycle. This is coherent with recent publications [37,72,73], which disclose increased overpotential in the presence of Zn(II). As far as the EIS measurements are concerned, for GDE A, the charge-transfer resistance is about doubled in the presence of zincates, right from the beginning of the test. The mass-transport resistance starts to grow since the anodic step at 40 mA cm^{-2} of the second cycle and, at the end of the test, it exhibits a value with is ca. a factor of four higher than with the zincate-free electrolyte. In addition, zincates exhibit an immediate impact on the evolution of electrocatalyst, since no training period can be observed at the beginning of the test.

The electrochemical tests of the GDE with 23 wt% Ni/NiO NPs (GDE C) in the absence and in the presence of zincates are reported in the bottom Panel of Fig. 3. The addition of Zn(II) does not bring about important changes in the ORR and OER overvoltges, showing a notable effect of Ni/NiO NPs on the stabilization of GDE performance with respect to Zn(II) contamination. The same message is conveyed by the evolution of the EIS spectra and, in particular, by the change of the series resistance (inset in bottom right Panel). The charge-transfer resistance is essentially the same in the absence and in the presence of zincates. The mass-transport resistance starts to grow at the same point of the test protocol (i.e. after completion of the low-c.d. steps of the third cycle) and, at the end of the experiment, it exhibits an approximately double value in the presence of zincates. EIS thus proves capable of detecting early zincate deterioration in a regime in which the potential time-series are still identical. The first EIS spectra show that the training effect that was suppressed by zincates for the Ni-free GDEs, is instead restored with 23 wt% Ni/NiO NPs.

In conclusion, our results reported in Fig. 3, on the one hand, confirm - for the case of GDEs aged in realistic conditions -, the impact of zincates that we pinpointed, on the basis of mere electroanalytical tests, in [45], and, on the other hand, disclose a notable stabilizing effect of Ni/NiO NPs.

3.3. Characterization of GDEs in pristine and post mortem conditions

The GDEs tested electrochemically as described in Section 3.2, have been inspected by SEM, STXSM and TEM analyses, to achieve an insightful understanding of their response to ORR and ORR/OER bifunctional operating conditions. *Post mortem* SEM has been firmly proved to be an appropriate method for the assessment of some aspects of the degradation of the AL of GDEs [43,74]. STXSM can detect the space distribution of the chemical state with submicrometer resolution, and has been extensively used by our group to follow the electrochemical behaviour of Mn-based ORR electrocatalysts [75–79]. TEM studies provide essential information on the nanostructural assessments of the samples with also insights on their chemical distribution down to atomic scale. Moreover, comparative analyses on the as-fabricated α-MnO_2 and the pristine GDEs have been performed to accurately assess the initial conditions of the electrochemical ageing process.

For SEM imaging, samples were washed in deionized water and isopropanol to remove the excess potassium salt from the surface. No loss of material was noticed during this step. The GDEs were then left to dry in still air and mounted on the SEM sample holder without any additional treatments. TEM and STXSM analyses were carried out on samples extracted from GDEs and detailed in Sections 2.3 and 2.4, respectively.

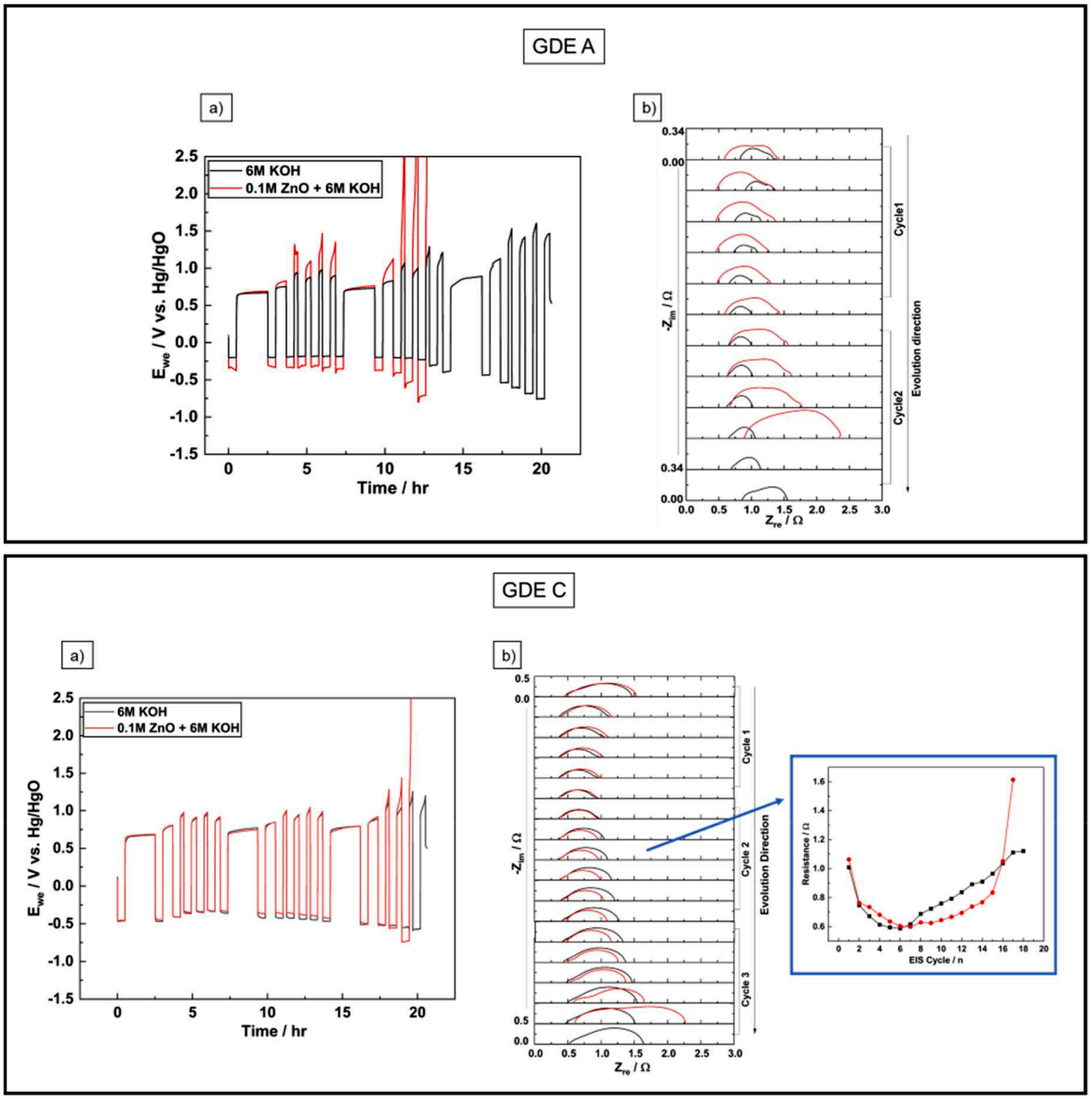

Fig. 3. Results of the OER/ORR rapid screening protocol (see Section 3.2.1 and Figure S7 of the Supporting Information) for GDEs without (GDE A) and with 23 wt% (GDE C) Ni/NiO NPs in zincate-free (red plots) and 0.1 M ZnO (black plots) electrolytes. (a) Potential responses to the galvanostatic test sequence; (b) EIS results (Nyquist plots). The EIS spectra for the case without zincate are reported only in the testing range relevant for comparison. The inset of the Panel containing EIS data for GDE C reports the series resistance as a function of cycle number.

3.3.1. SEM imaging

The GDEs were observed at low magnification, to assess the overall quality of the samples, - in particular to check the cracking that we have shown to correlate with loss of performances due to loss of hydrophobicity [43], and at high magnification, to check the morphological evolution of the electrocatalyst particles.

Figs. 4 and S9 in the Supporting Information compare SEM micrographs at low magnification for mono- and bifunctional GDEs in pristine conditions and after the electrochemical ageing protocol described in Sections 3.2.1 (no added Zn(II)) and 3.2.2 (with added Zn(II)), respectively. It is evident from these micrographs, that - coherently with our results of [69] - as a result of electrochemical cycling both in the absence and in the presence of Zn(II), the GDE undergoes cracking. In general, the development of a crack framework correlates with the increase of the mass-transport resistance highlighted in Section 3.2, in keeping with our results of [69] and similar conclusions of [80], based on flooding analysis. A closer look at the concentration and size of cracks for the GDEs without and with Ni/NiO NPs reveals a more complex scenario. Ni-containing GDEs exhibit a clear trend, whereby presence of Ni correlates with less extensive cracking. In the absence of Ni/NiO, instead, cracking is quite limited even though degradation of mass-transport is more severe, indicating that flooding of Ni-free GDEs is mainly controlled by oxidative attack of CB, Mn(III) species and PTFE, as confirmed by the XANES results reported in Section 3.3.3.

It is worth noting that no evident correlation can be established between the electrocatalyst or electrolyte compositions and the cracking pattern and density. This confirms that this kind of damaging is a system response of the whole AL architecture, probably involving some form of

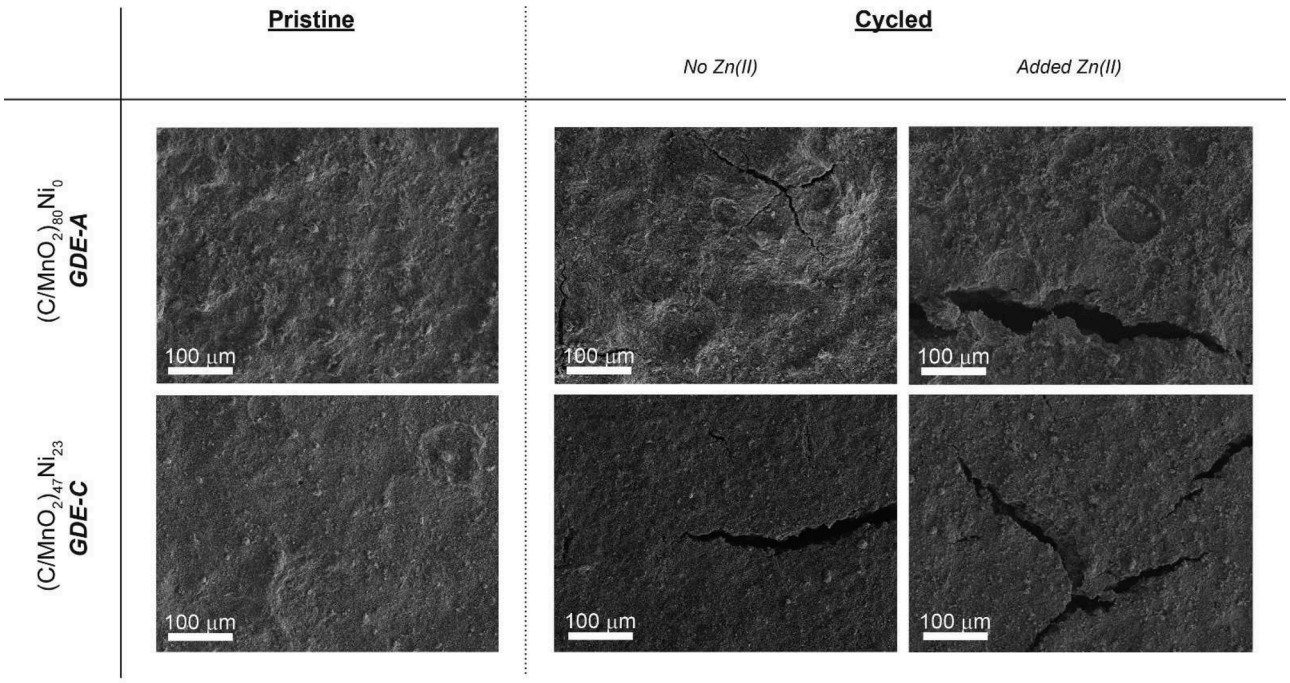

Fig. 4. SEM micrographs of the GDEs without (GDE A) and with 23 wt% Ni/NiO NPs (GDE C) in pristine conditions (left column), after electrochemical cycling in zincate-free 6 M KOH electrolyte (central column) and after electrochemical cycling in 6 M KOH + 0.1 M ZnO electrolyte (right column). For details, see Sections 3.2.1 and 3.2.2.

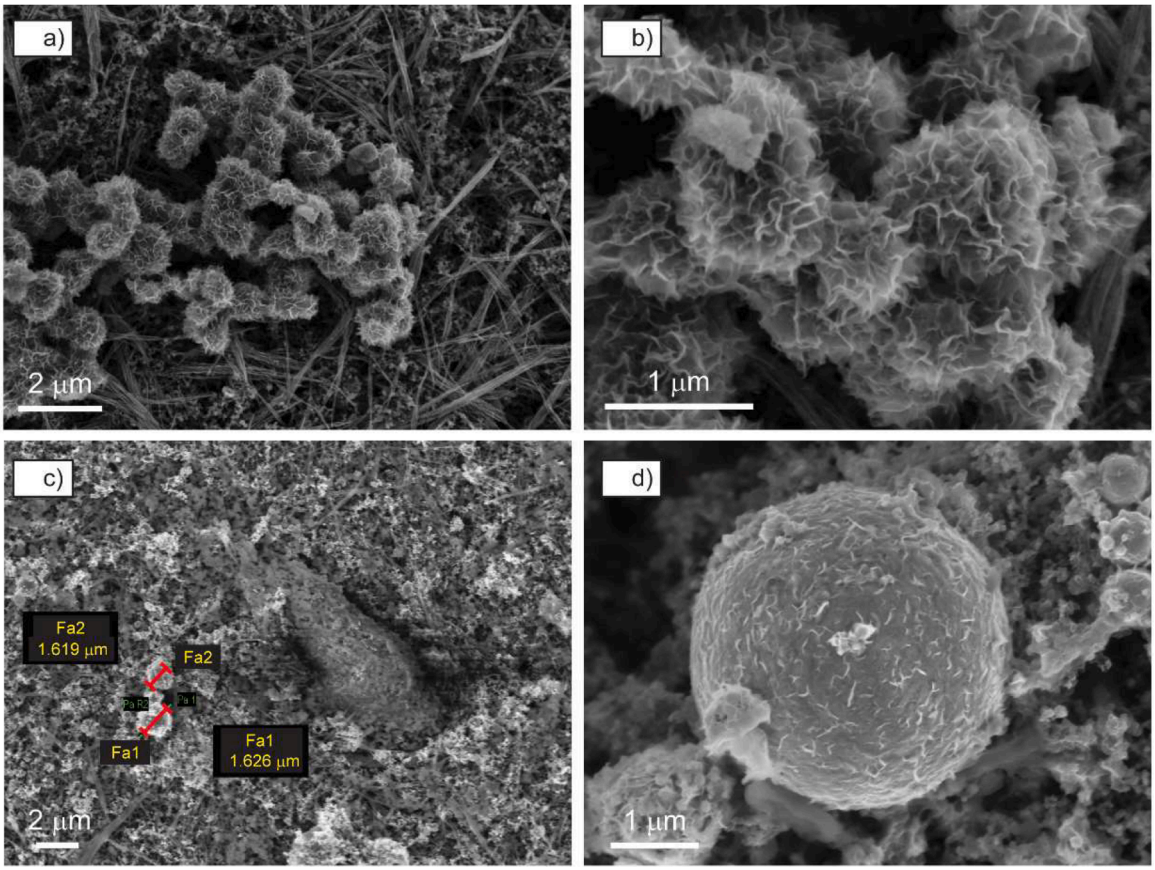

Fig. 5. (a, b) SEM micrographs at high magnification of the monofunctional GDE, after ORR/OER electrochemical cycling 6 M KOH electrolyte as described in Section 3.2.1. (c, d) SEM micrographs at high magnification of the bifunctional GDE with 23 wt% Ni/NiO NPs, after ORR/OER electrochemical cycling 6 M KOH electrolyte, as described in Section 3.2.1.

evolution of the interaction between the PTFE binder and the population of electrocatalyst and CB particles.

From the SEM micrographs at higher magnification, reported in Fig. 5, it can be observed that - coherently with our results of our more fundamental study of the Mn-based electrocatalyst reported in [45] - the microstructure of the α-MnO_2 nanowires is indeed affected by ageing, giving rise to less defined and thicker filaments, as well as to a thin layer of material encasing bundles of filament-shaped features. Since this shape change is common to all samples, it is not possible to draw definitive conclusions regarding the impact of GDE composition, based solely on SEM evidence. This morphological transformation is further highlighted in the HRTEM work described in Section 3.3.2 and its chemical-state counterpart is clarified through the XANES measurements presented in Section 3.3.3. In addition to changes in the shape of rod-like and filamentary features, monofunctional electrodes subjected to ORR/OER cycling in the 6 M KOH electrolyte, we also found the formation of micrometric globular Mn-containing crystallites, with plate-like substructures (Fig. 5(a,b)). Crystallites of this type are typical of electrodeposited MnO_2 [19] and can be explained with anodic electrodeposition, in the OER cycle at the high potentials that are observed in the absence of the Ni/NiO NPs, of MnO_x from solution Mn(II) dissolved from α-MnO_2 nanowires in the ORR cycles in the period in which high cathodic polarizations are caused by progressive GDE degradation. Also the Ni/NiO NPs undergo shape changes as a result of electrochemical ageing: these are visible in Fig. 5(a,b), referring to the bifunctional GDE with 23 wt% Ni/NiO NPs, but showing a scenario that is typical of all Ni-containing GDEs. The increase of Ni particle diameter from nanometric with a narrow dispersion (5–20 nm) to polydisperse with maximum diameters of 1–2 μm, is a result of Ostwald ripening, activated by the alternation of ORR and OER conditions leading, respectively, to the periodic reduction of the NiO shell, when coalescence is favoured. This mechanism brings about the loss of active sites and thus affects the electrochemical activity towards OER [81–83], causing a progressive increase of the anodic overvoltage that, in turn, activates carbon oxidation.

3.3.2. TEM imaging and structural analysis

As put forward in Section 3.3.1, TEM studies demonstrate the morphological and structural evolution of α-MnO_2 nanowires after ageing under ORR and ORR/OER conditions, without and with Zn(II) in the electrolyte. Bright-field (BF) TEM images of as-synthesized α-MnO_2 nanowires (Fig. 6(a)) and samples extracted from a pristine monofunctional GDE (Fig. 6(g)) show wire diameters of 20–30 nm, with a length of ca. 0.5 μm, as estimated from SEM images. Fig. 6(b) shows a representative high resolution TEM (HRTEM) image of a portion of nanowire, indicted by a red box in Fig. 6(a). The HRTEM image and the corresponding fast Fourier transform (FFT) pattern (inset of Fig. 6(b)), obtained from the area of the nanowire highlighted with the box, reveal that the nanowire has a single-crystalline cryptomelane structure. The chemical composition of the as-synthesized α-MnO_2 nanowires was assessed by STEM-EDS analysis. Representative HAADF STEM images of the α-MnO_2 nanowires are shown in Fig. 6(c) and the EDS elemental maps for Mn, O and K are presented in Fig. 6(d-e). The EDS maps show the presence of K, which is consistent with the intercalated into tunnel structure of cryptomelane. Fig. 6(g) also depicts CB spheroids, together with in α-MnO_2 nanowires. The HRTEM image of a portion of a single nanowire (Fig. 6(h)), and the corresponding FFT (Fig. 6(i)) obtained from the box region, confirm that the single-crystalline cryptomelane nature is preserved. These cryptomelane single-crystals transform into assemblies of amorphous flakes when the monofunctional GDEs are aged for a prolonged period under ORR conditions (Fig. 7(a)). Addition of Zn(II) (Fig. 7(b)) causes the transformation of α-MnO_2 single-crystals into polycrystalline Mn_2ZnO_4 crystallites, as confirmed by the HRTEM image (Fig. 7(c)) and the associated FFT pattern (inset of Panel c). The single-crystal cryptomelane structure is preserved (Fig. 7(d)) after ORR/OER cycling in the Zn(II)-free electrolyte, thanks to the stabilizing action of the anodic period towards the relevant Mn^{3+}/Mn^{4+} proportion, which is desirable for the catalyst to be efficient and reversible [84] (for chemical-state details, see Section 3.3.3). Instead, the presence of Zn(II) (Fig. 7(e)) causes the formation Mn_2ZnO_4 polycrystal cores, capped with a 10 nm thick amorphous shell. The HRTEM image and the corresponding FFT pattern (Fig. 7(f)) confirm the formation of Mn_2ZnO_4

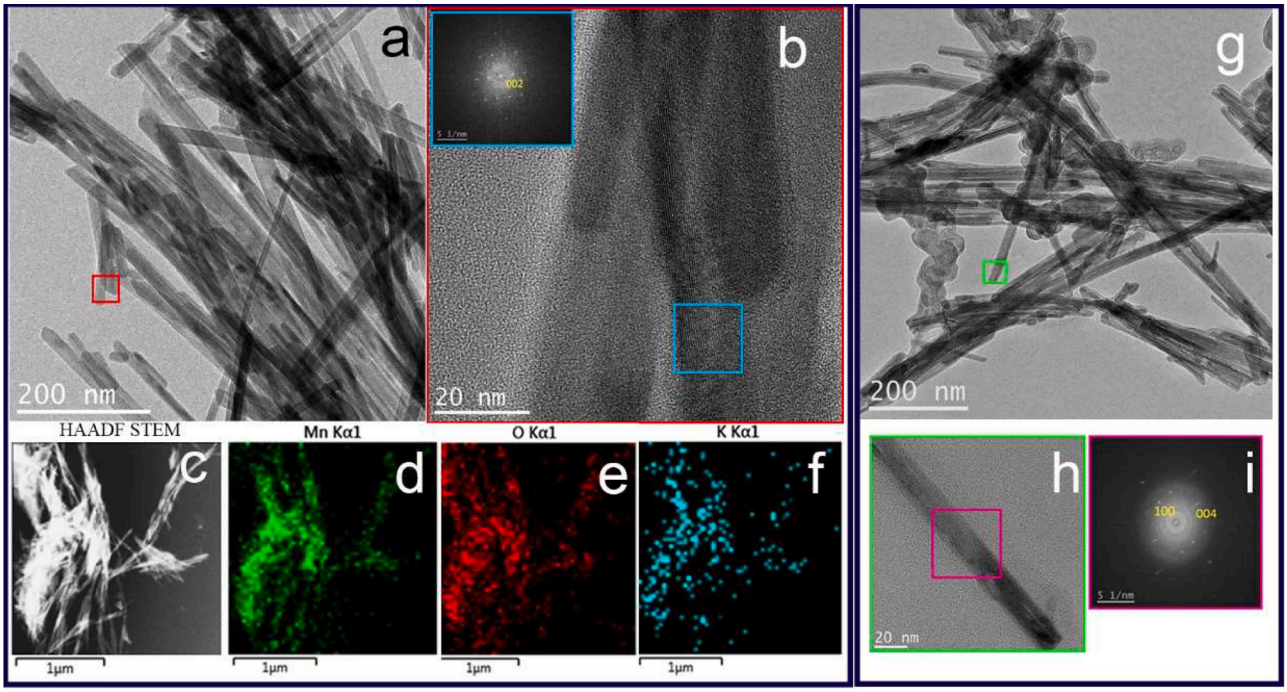

Fig. 6. (a) BF TEM and (b) HRTEM images of the as-synthesized α-MnO_2 nanowires. (c) HAADF-STEM image of as-synthesized α-MnO_2 nanowires and corresponding EDS maps for: Mn (Panel d), O (Panel e), and K (Panel f). (g) BF TEM and HRTEM of a sample extracted from a pristine GDE: (h) HRTEM image of a portion of a nanowire, (i) FFT associated to the region of Panel h, highlighted with the purple box.

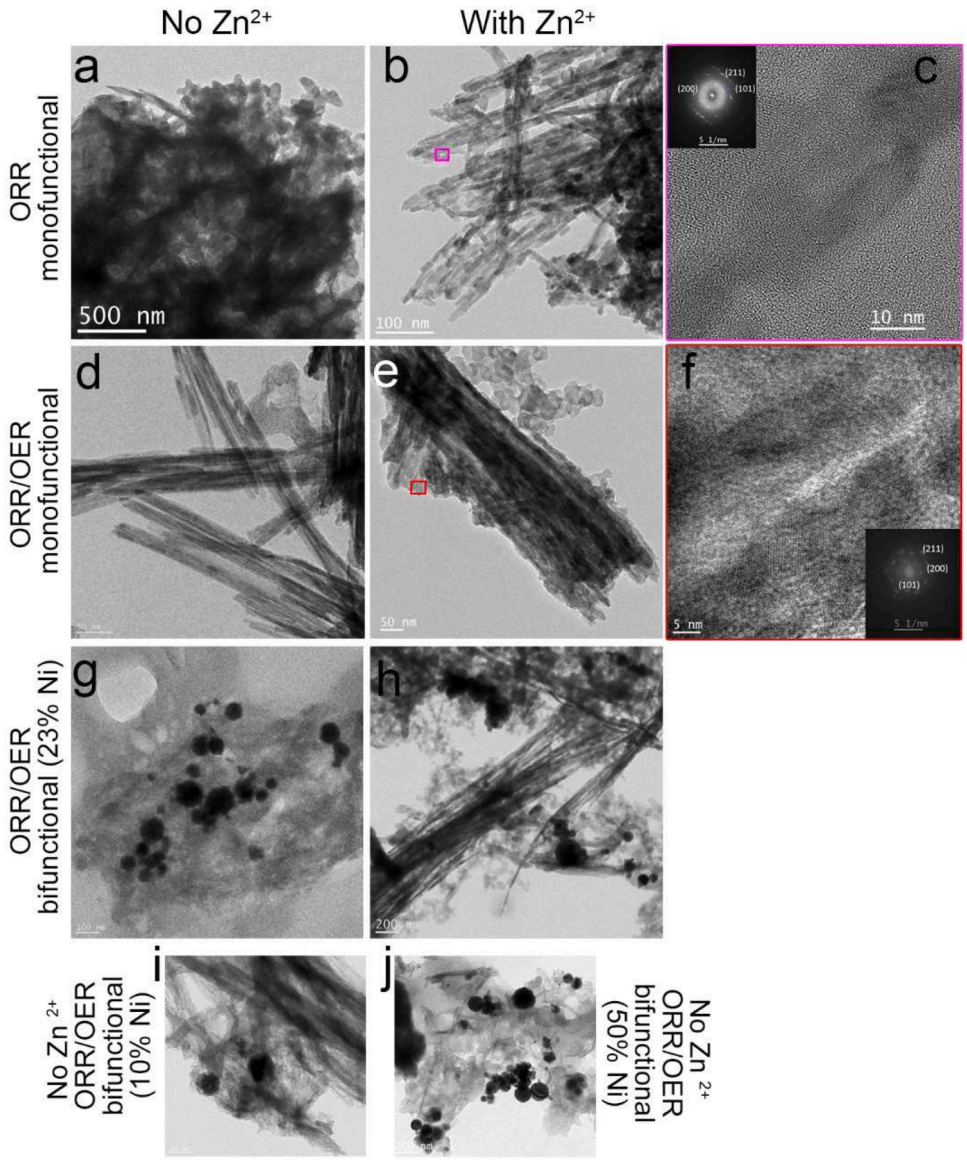

Fig. 7. (a, b, d, e, g, h, i, j) TEM images of electrocatalysts extracted from mono- and bifunctional GDEs aged under ORR and ORR/OER conditions in the Zn(II)-free (a, d, g, i, j) and in the Zn(II)-containing (b, e, h) electrolytes. (c, f) HRTEM images and the corresponding FFT patterns of the electrocatalyst extracted from the monofunctional GDE aged in the presence of Zn(II) under ORR (Panel c) and ORR/OER conditions (Panel f).

polycrystals. Thanks to the presence of Ni/NiO NPs in the bifunctional electrodes, α-MnO_2 nanowires tested in the Zn(II) free electrolyte (Fig. 7 (g)) exhibit the same kind of amorphization as the monofunctional GDEs tested under ORR conditions. This can be explained in two ways: firstly in terms of the reduction of oxidative stress provided by OER-electrocatalytic Ni/NiO NPs (see electrochemical results of Sections 3.1 and 3.2.2 and chemical-state information of Section 3.3.3), and, secondly, considering the cumulative reductive damaging of cryptomelane observed in (Fig. 7(a)). Bifunctional GDEs, subjected to ORR/OER cycling in presence of Zn(II) (Fig. 7(h)), undergo the same transformation into a core-shell structure with polycrystalline Mn_2ZnO_4 core and amorphous shell. The TEM results (Fig. 7(g-j)) confirm the Ostwald ripening of Ni/NiO NPs, as observed by SEM (Fig. 5(d)).

3.3.3. *Scanning soft-X ray transmission spectromicroscopy (STXSM)*

STXSM mapping at the Mn L-edge was carried out to gain insight into the chemical-state distribution and evolution of α-MnO_2 nanowires from the pristine state, to that resulting from ORR and ORR/OER cycling, without and with added Zn(II). Fig. 8 reports XANES spectra extracted from stacks of images for the different systems investigated, together with a typical absorption image. Accurate inspection of the stacks of images reveals that the chemical-state distribution over the Mn-containing features - essentially bundles of nanowires or fibers, modified by ageing - is essentially homogeneous: in-depth quantitative analysis, discloses some interesting deviations from homogeneity, that will be the object of discussion in a separate publication. For the present purpose, the key spectroscopic message is conveyed by the spectra reported in Panels (a)-(c) of Fig. 8, obtained by averaging over ten representative single-pixel spectra extracted from regions of the stacks of images showing reasonable absorption at the Mn L-edge. One can immediately note that significant changes of the chemical-state of Mn are brought about by the different processing and ageing conditions considered. Specifically, as synthesized α-MnO_2 (black plot) exhibits a mixture of Mn(III) and Mn(IV), which is coherent with K-intercalation into the tunnel structure of cryptomelane, as detailed above, in Section 3.3.2. α-MnO_2 extracted from the pristine GDE (red plot) shows the formation of Mn(II), that can be explained with carbothermal reduction taking place during the heat treatment step of GDE fabrication. In fact,

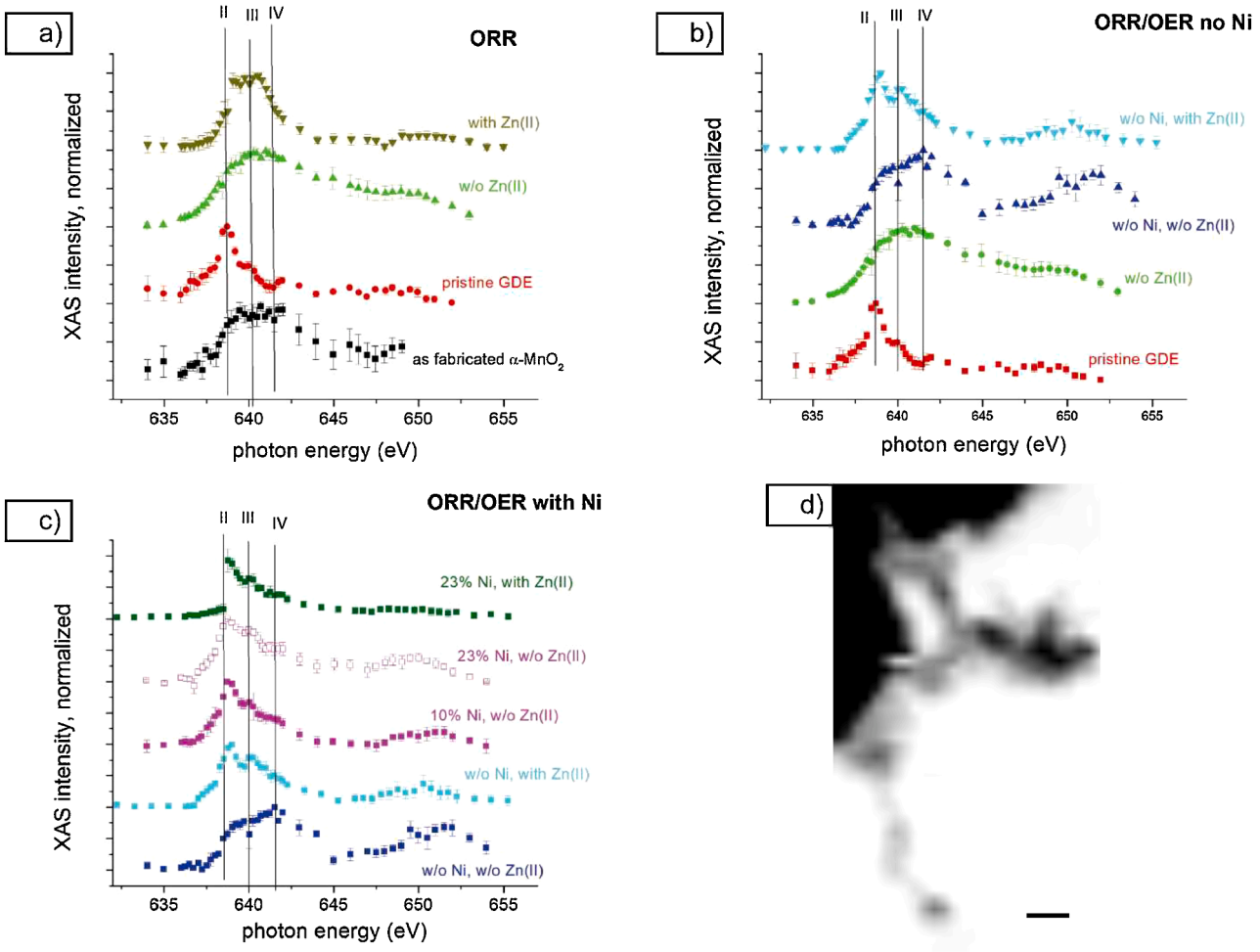

Fig. 8. (a-c) Mn L-edge X-ray absorption spectra extracted from stacks of images acquired from active-layer samples sampled from the indicated GDEs, aged under the electrochemical conditions specified in the image. (d) Typical absorption image (recorded at 637 eV) from the image stack for GDE with 23 wt% Ni/NiO, aged under ORR/OER conditions, in the presence of Zn(II). Scale bar is 2 μm.

the processing conditions are thermodynamically compatible with MnO_2 reduction to MnO [85]. Electrochemical cycling in ORR conditions in the absence of Zn(II) (green plot), showed that the electrochemical response restored the active Mn(III) + Mn(IV) mixture. This behaviour is coherent with the improvement of electrocatalytic performance during the initial period of electrochemical polarization (training effect) demonstrated in Section 3.2. In addition, the Mn valence states confirm the mechanism proposed in [84], in which the residual Mn(II) species after O_2 evolution are converted back to Mn(III), following a comproportionation reaction between Mn(II) and Mn(IV) species. Instead, the same test, carried out in the presence of Zn(II) (olive plot), shows the chemical-state of Mn shifted to a Mn(II) + Mn(III) mixture. This valence scenario is coeherent with the formation of mixed Zn-Mn oxides pinpointed in [45] and highlighted by the FFT plots in Section 3.3.2. Moreover, it is worth noting that the training effect tends to be suppressed by the addition of Zn(II) (Section 3.2.2). When the monofunctional GDE is subjected to ORR/OER cycles (blue plot), a higher concentration of Mn(IV) is found, coherently with the prevalence of higher anodic overvoltages. In these conditions, addition of Zn(II) (light blue plot), stabilizes Mn(II) and Mn(III), as we found in the ORR test: again, corresponding to formation of an inactive phase.

When the Ni-based GDEs were cycled in the absence of Zn(II) under ORR/OER conditions (magenta plots), a mixture of Mn(II) and Mn(III) is found. This chemical-state scenario, together with the fast-training effect of Ni/NiO NPs discussed in Section 3.2.1, suggests that the anodic potential control afforded by Ni, limits the conversion of pristine or retained solid Mn(II), thanks to the lower anodic potentials enabled by the OER electrocatalyst. On the one hand, Mn(II) tends to be preserved in solid form, thanks to the ORR electrocatalytic effect of α-MnO_2, that hinders cathodic dissolution to aqueous Mn(II) species, but, on the other hand, lower anodic potentials allow a lower conversion of this species to higher-valent forms, thus providing a reservoir of activable material. Lower anodic polarizations in the presence of Ni/NiO NPs -, stabilize electrocatalytically active Mn(III), avoiding anodic dissolution of the solid electrocatalyst to Mn(VI) and Mn(VII) alkaline aqueous compounds. More details on these aspects, supported by in-line VIS spectrometry, will be provided in a paper in preparation. As in the case of Ni-free GDEs, Zn(II) in the electrolyte correlates with an increase in the Mn (II) fraction (dark green plot), which, again, is related to irreversible phase transformation. Nevertheless, the electrochemical results of Section 3.2.2 show that the addition of Zn(II) does not bring about important changes in the ORR and OER performance, showing a notable effect of Ni/NiO NPs on the stabilization of GDE performance with respect to Zn(II) contamination, and a lower propensity to the formation of Zn-Mn mixed oxides in the presence of Ni/NiO NPs, as proved by the structural analyses of Section 3.3.2.

4. Conclusions

This paper describes a novel fabrication protocol for the reversible oxygen electrode of an electrically rechargeable Zn-air battery. The fabrication process includes: microwave-assisted hydrothermal

synthesis of α-MnO_2 nanowires – the ORR electrocatalyst –, formulation of the precursor ink for the AL, including α-MnO_2 and Ni/NiO NPs (the OER electrocatalyst), spray-coating of the AL onto carbon paper and final thermal-treatment to optimize hydrophobicity. Different Ni-based compositions were evaluated to find the optimal GDE. The electrocatalytic performance of the AL was evaluated by voltammetry at RDE/RRDE. As expected, no impact of Ni/NiO NPs was found on the ORR process, that is invariably a 4-electron mechanism, but the Ni/NiO NP-containing ALs exhibits a better performance, owing to improved electronic conductivity. The fabricated GDEs were tested with a comprehensive range of electrochemical methods – galvanostatic sequences and EIS in half-cell configuration, including the evaluation of ageing effects upon successive galvanostatic charge-discharge cycling. The characterization of pristine and aged GDEs was completed by *post mortem* SEM, TEM and STXSM. Finally, the impact of the presence of Zn(II) in the electrolyte on the GDE performance was assessed. All fabricated GDEs enable the attainment of remarkably high ORR c.d.s, in excess of 200 mA cm^{-2}, below the voltage cutoff, and exhibit good electrocatalytic performance and stability upon ORR/OER cycling. Addition of Ni/NiO NPs leads to lower anodic overvoltages, that converts in lower propensity to carbon-support corrosion, in turn leading to lower cathodic overvoltages and better overall stability of the GDE. The presence of Zn(II) in the electrolyte causes accelerated failure of the GDEs, owing to the formation of inactive Zn-Mn-containing phases: presence of Ni attenuates the obnoxious effect of zincates. Within the investigated compositional range, the fraction of Ni/NiO NPs correlates with an improvement of bifunctional performance, with a major impact of composition increasing from 10 to 23 wt% Ni/NiO NPs and tending to level off at 50 wt%.

SEM analysis showed that electrochemical ageing leads to the development of cracking of the GDEs. SEM Imaging at high magnification disclosed that the morphology of α-MnO_2 nanowires is affected by ageing, leading to the formation of bundles of poorly defined filaments. This observation is confirmed by TEM, which discloses the formation of amorphous regions in all GDEs investigated. Moreover, Mn-containing globular crystallites appear, resulting from anodic electrodeposition of MnO_2 from Mn(II) dissolved in the cathodic cycles. Finally, Ni/NiO NPs undergo significant Ostwald under OER/ORR cycling. These structural changes of both MnO_2 and Ni particles correlate with the degradation of electrocataytic performance.

Finally, the nature and space distribution of the chemical state of Mn, as a function of GDE composition and ageing conditions, was assessed by STXSM at the Mn L-edge. The chemical-state distribution was found to be homogeneous on the micrometric and submicrometric scale. In bifunctional GDEs, balanced Mn(III) and Mn(IV) contents were found to correlate with electrocatalytic activity, while the presence of Mn(II) corresponds to activity depression either in the as-fabricated state – that requires a training period to attain optimal performance – or to loss of activity due to the formation of parasitic Zn-Mn-containing phases, confirmed by TEM. In the bifunctional GDEs - in which Ni/NiO NPs enable OER activity at lower anodic potentials -, better electrocatalytic performance correlates with the stabilization of active Mn(III), as well as with the presence of a fraction of untransformed Mn(II), which can act as a reservoir of active material partially compensating the degradation of GDE performance. Also with Ni-containing GDE, presence of Zn(II) leads to the formation of inactive phases – as witnessed by higher fractions of Mn(II), TEM imaging –, but their performance is more stable in comparison with their monofunctional counterpart, owing to lower overvoltages in both the anodic and cathodic branches.

In conclusion, it is worth noting that the fabrication protocol proposed, comprising microwave-assisted synthesis and spray coating, demonstrates evident cost-effectiveness for the demonstration and scale-up scales and objectives of current interest for EZAB science and technology. Transitioning to mass production would naturally lean towards more traditional, large-batch methods like hydrothermal synthesis and doctor blading.

Credit author statement

All authors contributed equally to: (i) conceptualization, (ii) methodology, (iii) software, (iv) validation, (v) formal analysis, (vi) investigation, (vii) data curation, (vii) all stages of writing and (viii) visualisation, with the following exceptions: (a) in addition to the previously mentioned contributions (i)-(viii), Yawar Salman and Sheharyar Waseem equally deployed a relatively larger experimental effort in carrying out GDE preparation and electrochemical testing; (b) in addition to the previously mentioned contributions (i)-(viii), Benedetto Bozzini also globally coordinated and supervised the research project.

Declaration of Competing Interest

The authors declare the following financial interests/personal relationships which may be considered as potential competing interests:

Benedetto Bozzini reports financial support was provided by European Commission. Andrea Li Bassi reports financial support was provided by European Commission.

Data availability

Data will be made available on request.

Acknowledgments

Benedetto Bozzini acknowledges funding by:

MOST – Sustainable Mobility center and received funding from the European Union Next-GenerationEU (PIANO NAZIONALE DI RIPRESA E RESILIENZA (PNRR) – MISSIONE 4 COMPONENTE 2, INVESTIMENTO 1.4 – D.D. 1033 17/06/2022, CN00000023).

Andrea Li Bassi acknowledges funding by:

• Funder: Project funded under the National Recovery and Resilience Plan (NRRP), Mission 4 Component 2 Investment 1.3 - Call for tender No. 1561 of 11.10.2022 of Ministero dell'Università e della Ricerca (MUR); funded by the European Union – NextGenerationEU.

• Award Number: Project code PE0000021, Concession Decree No. 1561 of 11.10.2022 adopted by Ministero dell'Università e della Ricerca (MUR), CUP D43C22003090001, Project title "Network 4 Energy Sustainable Transition – NEST".

This manuscript reflects only the authors' views and opinions, neither the European Union nor the European Commission can be considered responsible for them.

Supplementary materials

Supplementary material associated with this article can be found, in the online version, at doi:10.1016/j.electacta.2023.143246.

References

[1] S.I. Smedley, X.G. Zhang, A regenerative zinc–air fuel cell, J. Power Sources 165 (2) (2007) 897–904.
[2] M. Winter, B. Barnett, K. Xu, Before li ion batteries, Chem. Rev. 118 (23) (2018) 11433–11456.
[3] J. Zhang, Q. Zhou, Y. Tang, L. Zhang, Y. Li, Zinc–air batteries: are they ready for prime time? Chem. Sci. 10 (2019) 8924–8929.
[4] J. Fu, Z. P.Cano, M.G. Park, A. Yu, M. Fowler, Z. Chen, Electrically rechargeable zinc–air batteries: progress, challenges, and perspectives, Adv. Mater. 29 (7) (2017), 1604685.
[5] Y. Li, J. Lu, Metal–air batteries: will they be the future electrochemical energy storage device of choice? ACS Energy Lett. 2 (6) (2017) 1370–1377.
[6] J. Yang, S. Park, K.Y. Choi, H. Park, Y. Cho, H. Ko, H. Song, Activity-durability coincidence of oxygen evolution reaction in the presence of carbon corrosion: case study of $MnCo_2O_4$ spinel with carbon black, ACS Sustain. Chem. Eng. 6 (8) (2018) 9566–9571.
[7] L. Wang, J. Zheng, Recent advances in cathode materials of rechargeable aqueous zinc-ion batteries, Mater. Today Adv. 7 (2020), 100078.

[8] J. Lee, S.T. Kim, R. Cao, N. Choi, M. Liu, K.T. Lee, J. Cho, Metal–air batteries with high energy density: li–air versus Zn–air, Adv. Energy Mater. 1 (1) (2011) 34–50.

[9] A.K. Worku, D.W. Ayele, N.G. Habtu, M.A. Teshager, Z.G. Workineh, Recent progress in MnO_2-based oxygen electrocatalysts for rechargeable Zinc-air batteries, Mater. Today Sustain. 13 (2021), 100072.

[10] A. Ikezawa, K. Seki, H. Arai, Design of bifunctional air electrodes based on the reaction fields between oxygen reduction reaction and oxygen evolution reaction, Electrochim. Acta 394 (2021), 139128.

[11] F. Cheng, J. Chen, Metal–air batteries: from oxygen reduction electrochemistry to cathode catalysts, Chem. Soc. Rev. 41 (2012) 2172–2192.

[12] D.U. Lee, P. Xu, Z.P. Cano, A.G. Kashkooli, M.G. Park, Z. Chen, Recent progress and perspectives on bi-functional oxygen electrocatalysts for advanced rechargeable metal–air batteries, J. Mater. Chem. A 4 (2016) 7107–7134.

[13] E. Davari, D.G. Ivey, Bifunctional electrocatalysts for Zn–air batteries, Sustain. Energy Fuels 2 (2018) 39–67.

[14] L. Jörissen, Bifunctional oxygen/air electrodes, J. Power Sources 155 (1) (2006) 23–32.

[15] Y. Takeshita, S. Fujimoto, M. Sudoh, Design of rechargeable air diffusion cathode for metal-air battery using alkaline solution, ECS Trans. 50 (19) (2013) 3.

[16] W. Tian, J. Ren, X. Lv, Z. Yuan, A "gasbreathing" integrated air diffusion electrode design with improved oxygen utilization efficiency for high-performance Zn-air batteries, Chem. Eng. J. 431 (2022), 133210.

[17] P. Li, C. Hu, T. Lee, W. Chang, T.H. Wang, Synthesis and characterization of carbon black/manganese oxide air cathodes for zinc-air batteries, J. Power Sources 269 (2014) 88–97.

[18] Y. Kumar, S. Chopra, A. Gupta, Y. Kumar, S.J. Uke, S.P. Mardikar, Low temperature synthesis of MnO_2 nanostructures for supercapacitor application, Mater. Sci. Energy Technol. 3 (2020) 566–574.

[19] J. Shin, J.K. Seo, R. Yaylian, A. Huang, Y.S. Meng, A review on mechanistic understanding of MnO_2 in aqueous electrolyte for electrical energy storage systems, Int. Mater. Rev. 65 (6) (2020) 356–387.

[20] X. Jin, Y. Xie, C. Zhao, Y. Xu, Y. Lv, H. Wang, L. Chen, J. Huang, FeCo-based mesoporous carbon shells modified n-doped porous carbon spheres for oxygen reduction reaction, Progr. Natural Sci.: Mater. Int. 31 (4) (2021) 527–535.

[21] Y. Gao, D. Zheng, Q. Li, W. Xiao, T. Ma, Y. Fu, Z. Wu, L. Wang, 3D Co_3O_4-RuO_2 hollow spheres with abundant interfaces as advanced trifunctional electrocatalyst for water-splitting and flexible Zn–air battery, Adv. Funct. Mater. 32 (38) (2022), 2203206.

[22] D. Liu, L. Qiao, Y. Chen, P. Zhou, J. Feng, C.C. Leong, K.W. Ng, S. Peng, S. Wang, W.F. Ip, H. Pan, Electrocatalytic reduction of nitrate to ammonia on low-cost manganese-incorporated Co_3O_4 nanotubes, Appl. Catal. B: Environ. 324 (2023), 122293.

[23] V. Caramia, B. Bozzini, Materials science aspects of zinc–air batteries: a review, Mater. Renew. Sustain. Energy 3 (2) (2014) 28.

[24] H. Li, X. Li, Q. Nie, K. Lian, J. Qiao, MnO_2 nanotubes synthesized with one-step hydrothermal method as efficient bi-functional cathode catalyst for a rechargeable zinc-air battery, in: Proceedings of the 2017 6th International Conference on Energy, Environment and Sustainable Development (ICEESD 2017), Atlantis Press, 2017, pp. 920–924.

[25] Y. Gu, G. Yan, Y. Lian, P. Qi, Q. Mu, C. Zhang, Z. Deng, Y. Peng, Mn^{III}-enriched -MnO_2 nanowires as efficient bifunctional oxygen catalysts for rechargeable Zn-air batteries, Energy Storage Mater. 23 (2019) 252–260.

[26] K. Selvakumar, S.M.S. Kumar, R. Thangamuthu, K. Ganesan, P. Murugan, P. Rajput, S.N. Jha, D. Bhattacharyya, Physiochemical investigation of shape-designed MnO_2 nanostructures and their influence on oxygen reduction reaction activity in alkaline solution, J. Phys. Chem. C 119 (12) (2015) 6604–6618.

[27] Y.L. Cao, H.X. Yang, X.P. Ai, L.F. Xiao, The mechanism of oxygen reduction on MnO_2-catalyzed air cathode in alkaline solution, J. Electroanal. Chem. 557 (2003) 127–134.

[28] F. Cheng, Y. Su, J. Liang, Z. Tao, J. Chen, MnO_2-based nanostructures as catalysts for electrochemical oxygen reduction in alkaline media, Chem. Mater. 22 (3) (2010) 898–905.

[29] Y. Huang, Y. Lin, W. Li, Controllable syntheses of - and - MnO_2 as cathode catalysts for zinc-air battery, Electrochim. Acta 99 (2013) 161–165.

[30] Y. Meng, W. Song, H. Huang, Z. Ren, S. Chen, S.L. Suib, Structure–property relationship of bifunctional MnO_2 nanostructures: highly efficient, ultra-stable electrochemical water oxidation and oxygen reduction reaction catalysts identified in alkaline media, J. Am. Chem. Soc. 136 (32) (2014) 11452–11464.

[31] M. Wang, K. Chen, J. Liu, Q. He, G. Li, F. Li, Efficiently enhancing electrocatalytic activity of MnO_2 nanorods/n-doped ketjenblack carbon for oxygen reduction reaction and oxygen evolution reaction using facile regulated hydrothermal treatment, Catalysts 8 (4) (2018).

[32] N. Govindarajan, M.T.M. Koper, E.J. Meijer, F. Calle-Vallejo, Outlining the scaling-based and scaling-free optimization of electrocatalysts, ACS Catal. 9 (5) (2019) 4218–4225.

[33] B. Bozzini, G. Kourousias, D.E. Bedolla, A. Gianoncelli, Chemicalstate evolution of Ni in MnNi/polypyrrole nanocomposites under bifunctional air electrode conditions, investigated by quasi-in situ multi-scale soft x-ray absorption spectroscopy, Mater. Today Energy 6 (2017) 154–163.

[34] M. Prabu, P. Ramakrishnan, H. Nara, T. Momma, T. Osaka, S. Shanmugam, Zinc–air battery: understanding the structure and morphology changes of graphene-supported $CoMn_2O_4$ bifunctional catalysts under practical rechargeable conditions, ACS Appl. Mater. Interfaces 6 (19) (2014) 16545–16555.

[35] Z. Chen, A. Yu, R. Ahmed, H. Wang, H. Li, Z. Chen, Manganese dioxide nanotube and nitrogen-doped carbon nanotube based composite bifunctional catalyst for rechargeable zinc-air battery, Electrochim. Acta 69 (2012) 295–300.

[36] J. Pan, Y.Y. Xu, H. Yang, Z. Dong, H. Liu, B.Y. Xia, Advanced architectures and relatives of air electrodes in Zn–air batteries, Adv. Sci. 5 (4) (2018), 1700691.

[37] A.R. Mainar, L.C. Colmenares, O. Leonet, F. Alcaide, J.J. Iruin, S. Weinberger, V. Hacker, E. Iruin, I. Urdanpilleta, J.A. Blazquez, Manganese oxide catalysts for secondary zinc air batteries: from electrocatalytic activity to bifunctional air electrode performance, Electrochim. Acta 217 (2016) 80–91.

[38] T.N. Lambert, J.A. Vigil, S.E. White, C.J. Delker, D.J. Davis, M. Kelly, M. T. Brumbach, M.A. Rodriguez, B.S. Swartzentruber, Understanding the effects of cationic dopants on MnO_2 oxygen reduction reaction electrocatalysis, The J. Phys. Chem. C 121 (5) (2017) 2789–2797.

[39] V. Vij, S. Sultan, A.M. Harzandi, A. Meena, J.N. Tiwari, W. Lee, T. Yoon, K.S. Kim, Nickel-based electrocatalysts for energy-related applications: oxygen reduction, oxygen evolution, and hydrogen evolution reactions, ACS Catal. 7 (10) (2017) 7196–7225.

[40] X. Li, D. Pletcher, A.E. Russell, F.C. Walsh, R.G.A. Wills, S.F. Gorman, S.W.T. Price, S.J. Thompson, A novel bifunctional oxygen GDE for alkaline secondary batteries, Electrochem. Commun. 34 (2013) 228–230.

[41] Y. Zhang, X. Teng, Z. Ma, R. Wang, W. Lau, A. Shan, Cu_2O-templated fabrication of $Ni(OH)_2{\cdot}0{\cdot}75H_2O$ hollow tubes for electrocatalytic oxygen evolution reaction, Progr. Natural Sci.: Mater. Int. 32 (5) (2022) 554–560.

[42] E. Marini, L. Jörissen, S. Brimaud, Rational design of a low-cost, durable and efficient bifunctional oxygen electrode for rechargeable metal-air batteries, J. Power Sources 482 (2021), 228900.

[43] E. Marini, M. Liebert, F. Rossi, D.O. De Souza, P. Baumli, G. Aquilanti, F. Regnet, I. Lüdeking, B. Bozzini, L. Jörissen, S. Brimaud, Mapping of the degradation processes at bifunctional O_2 gas diffusion electrode for aqueous alkaline metal-air batteries, J. Power Sources 546 (2022), 231879.

[44] E. Marini, D.O. De Souza, G. Aquilanti, M. Liebert, F. Rossi, B. Bozzini, Operando XAS of a bifunctional gas diffusion electrode for Zn-air batteries under realistic application conditions, Appl. Sci. 11 (24) (2021).

[45] F. Rossi, E. Marini, M. Boniardi, A. Casaroli, A.Li Bassi, A. Macrelli, C. Mele, B. Bozzini, What happens to MnO_2 when it comes in contact with Zn^{2+}? an electrochemical study in aid of Zn/MnO_2-based rechargeable batteries, Energy Technol. 10 (8) (2022), 2200084.

[46] L.R. Pahalagedara, S. Dharmarathna, C.K. King'ondu, M.N. Pahalagedara, Y.-T. Meng, C.-H. Kuo, S.L. Suib, Microwave-assisted hydrothermal synthesis of MnO_2: lattice expansion via rapid temperature ramping and framework substitution, J. Phys. Chem. C 118 (35) (2014) 20363–20373.

[47] F. Lufrano, E. Passalacqua, G. Squadrito, A. Patti, L. Giorgi, Improvement in the diffusion characteristics of low Pt-loaded electrodes for PEFCs, J. Appl. Electrochem. 29 (4) (1999) 445–448.

[48] J.M. Song, S.Y. Cha, W.M. Lee, Optimal composition of polymer electrolyte fuel cell electrodes determined by the ac impedance method, J. Power Sources 94 (1) (2001) 78–84.

[49] A. Pozio, A. Cemmi, M. Carewska, C. Paoletti, F. Zaza, Characterization of Gas Diffusion Electrodes for Polymer Electrolyte Fuel Cells, J. Fuel Cell Sci. Technol. 7 (4) (2010), 041003.

[50] D. Su, H.-J. Ahn, G. Wang, Hydrothermal synthesis of α-MnO_2 and β-MnO_2 nanorods as high capacity cathode materials for sodium ion batteries, J. Mater. Chem. A 1 (2013) 4845–4850.

[51] A.S. Poyraz, J. Huang, C.J. Pelliccione, X. Tong, S. Cheng, L. Wu, Y. Zhu, A. C. Marschilok, K.J. Takeuchi, E.S. Takeuchi, Synthesis of cryptomelane type α-MnO_2 ($K_xMn_8O_{16}$) cathode materials with tunable K^+ content: the role of tunnel cation concentration on electrochemistry, J. Mater. Chem. A 5 (2017) 16914–16928.

[52] M.A. Butt, Thin-film coating methods: a successful marriage of high-quality and cost-effectiveness—a brief exploration, Coatings 12 (8) (2022) 1115.

[53] S.T. Navale, V.V. Mali, S.A. Pawar, R.S. Mane, M. Naushad, F.J. Stadler, V.B. Patil, Electrochemical supercapacitor development based on electrodeposited nickel oxide film, RSC Adv. 5 (2015) 51961–51965, https://doi.org/10.1039/C5RA07953E.

[54] S.D. Dhas, P.S. Maldar, M.D. Patil, A.B. Nagare, M.R. Waikar, R.G. Sonkawade, A. V. Moholkar, Synthesis of NiO nanoparticles for supercapacitor application as an efficient electrode material, Vacuum 181 (2020), 109646.

[55] A. Gianoncelli, G. Kourousias, L. Merolle, M. Altissimo, A. Bianco, Current status of the TwinMic beamline at Elettra: a soft X-ray transmission and emission microscopy station, J. Synchrotron Radiat. 23 (6) (2016) 1526–1537.

[56] J. Melder, W.L. Kwong, D. Shevela, J. Messinger, P. Kurz, Electrocatalytic water oxidation by MnO_x/C: in situ catalyst formation, carbon substrate variations, and direct O_2/CO_2 monitoring by membrane-inlet mass spectrometry, ChemSusChem 10 (22) (2017) 4491–4502.

[57] H. Antoni, W. Xia, J. Masa, W. Schuhmann, M. Muhler, Tuning the oxidation state of manganese oxide nanoparticles on oxygen- and nitrogen-functionalized carbon nanotubes for the electrocatalytic oxygen evolution reaction, Phys. Chem. Chem. Phys. 19 (2017) 18434–18442.

[58] H. Antoni, D.M. Morales, Q. Fu, Y. Chen, J. Masa, W. Schuhmann, M. Muhler, Oxidative deposition of manganese oxide nanosheets on nitrogen-functionalized carbon nanotubes applied in the alkaline oxygen evolution reaction, ACS Omega 3 (9) (2018) 11216–11226.

[59] K. Mette, A. Bergmann, J. Tessonnier, M. Hävecker, L. Yao, T. Ressler, R. Schlögl, P. Strasser, M. Behrens, Nanostructured manganese oxide supported on carbon nanotubes for electrocatalytic water splitting, ChemCatChem 4 (6) (2012) 851–862.

[60] P. Pei, K. Wang, Z. Ma, Technologies for extending zinc–air battery's cyclelife: a review, Appl. Energy 128 (2014) 315–324.

[61] P. Gu, M. Zheng, Q. Zhao, X. Xiao, H. Xue, H. Pang, Rechargeable zinc–air batteries: a promising way to green energy, J. Mater. Chem. A 5 (2017) 7651–7666.
[62] J.-F. Drillet, F. Holzer, T. Kallis, S. Müller, V.M. Schmidt, Influence of CO_2 on the stability of bifunctional oxygen electrodes for rechargeable zinc/air batteries and study of different CO_2 filter materials, Phys. Chem. Chem. Phys. 3 (2001) 368–371.
[63] E. Gülzow, Alkaline fuel cells: a critical view, J. Power Sources 61 (1) (1996) 99–104.
[64] D. Schröder, U. Krewer, Model based quantification of aircomposition impact on secondary zinc air batteries, Electrochim. Acta 117 (2014) 541–553.
[65] M. Inaba, A.W. Jensen, G.W. Sievers, M. Escudero-Escribano, A. Zana, M. Arenz, Benchmarking high surface area electrocatalysts in a gas diffusion electrode: measurement of oxygen reduction activities under realistic conditions, Energy Environ. Sci. 11 (2018) 988–994.
[66] M.A. Al-Saleh, S. Gültekin, A.S. Al-Zakri, H. Celiker, Effect of carbon dioxide on the performance of Ni/PTFE and Ag/PTFE electrodes in an alkaline fuel cell, J. Appl. Electrochem. 24 (6) (1994) 575–580.
[67] X. Fan, Z. Yang, X. Xie, W. Long, R. Wang, Z. Hou, The electrochemical behaviors of Zn–Al–La-hydrotalcite in Zn–Ni secondary cells, J. Power Sources 241 (2013) 404–409.
[68] Z. Zhao, X. Fan, J. Ding, W. Hu, C. Zhong, J. Lu, Challenges in zinc electrodes for alkaline zinc–air batteries: obstacles to commercialization, ACS Energy Lett. 4 (9) (2019) 2259–2270.
[69] S. Ozcan, M. Tokur, T. Cetinkaya, A. Guler, M. Uysal, M.O. Guler, H. Akbulut, Free standing flexible graphene oxide + MnO_2 composite cathodes for li–air batteries, Solid State Ionics 286 (2016) 34–39.
[70] Z.M. Chan, D.A. Kitchaev, J.N. Weker, C. Schnedermann, K. Lim, G. Ceder, W. Tumas, M.F. Toney, D.G. Nocera, Electrochemical trapping of metastable Mn^{3+} ions for activation of MnO_2 oxygen evolution catalysts, Proc. Natl. Acad. Sci. 115 (23) (2018) E5261–E5268.
[71] J.F. Parker, J.S. Ko, D.R. Rolison, J.W. Long, Translating materials-level performance into device-relevant metrics for zinc-based batteries, Joule 2 (12) (2018) 2519–2527.
[72] A.A. Mohamad, Zn/gelled 6M KOH/O_2 zinc–air battery, J. Power Sources 159 (1) (2006) 752–757.
[73] H. Kim, E. Kim, S. Kim, H. Shin, Influence of ZnO precipitation on the cycling stability of rechargeable Zn–air batteries, J. Appl. Electrochem. 45 (4) (2015) 335–342.
[74] D. Aasen, M.P. Clark, D.G. Ivey, Investigation of transition metal-based (Mn, Co, Ni, Fe) trimetallic oxide nanoparticles on n-doped carbon nanotubes as bifunctional catalysts for Zn-air batteries, J. Electrochem. Soc. 167 (4) (2020), 040503.
[75] B. Bozzini, A. Gianoncelli, B. Kaulich, C. Mele, M. Prasciolu, M. Kiskinova, Electrodeposition of manganese oxide from eutectic urea/choline chloride ionic liquid: an in situ study based on soft x-ray spectromicroscopy and visible reflectivity, J. Power Sources 211 (2012) 71–76.
[76] C. Mele, M. Catalano, A. Taurino, B. Bozzini, Electrochemical fabrication of nanoporous gold-supported manganese oxide nanowires based on electrodeposition from eutectic urea/choline chloride ionic liquid, Electrochim. Acta 87 (2013) 918–924.
[77] B. Bozzini, P. Bocchetta, B. Alemán, M. Amati, A. Gianoncelli, L. Gregoratti, H. Sezen, A. Taurino, M. Kiskinova, Electrodeposition and pyrolysis of Mn/polypyrrole nanocomposites: a study based on soft x-ray absorption, fluorescence and photoelectron microspectroscopies, J. Mater. Chem. A 3 (2015) 19155–19167.
[78] B. Bozzini, P. Bocchetta, A. Gianoncelli, C. Mele, M. Kiskinova, Electrodeposition and ageing of Mn-based binary composite oxygen reduction reaction electrocatalysts, ChemElectroChem 2 (10) (2015) 1541–1550.
[79] A. Gianoncelli, I. Sgura, P. Bocchetta, D. Lacitignola, B. Bozzini, High-lateral resolution x-ray fluorescence microspectroscopy and dynamic mathematical modelling as tools for the study of electrodeposited electrocatalysts, X-Ray Spectrom. 44 (4) (2015) 263–275.
[80] Z.P. Cano, M.G. Park, D.U. Lee, J. Fu, H. Liu, M. Fowler, Z. Chen, New interpretation of the performance of nickel-based air electrodes for rechargeable zinc–air batteries, J. Phys. Chem. C 122 (35) (2018) 20153–20166.
[81] H. Wang, Z. Zhou, Q. Yuan, N. Tian, S. Sun, Pt nanoparticle netlike-assembly as highly durable and highly active electrocatalyst for oxygen reduction reaction, Chem. Commun. 47 (2011) 3407–3409.
[82] Y. Dai, J. Yu, M. Ni, Z. Shao, Rational design of spinel oxides as bifunctional oxygen electrocatalysts for rechargeable Zn-air batteries, Chem. Phys. Rev. 1 (1) (2020), 011303.
[83] S. Popović, M. Smiljanić, P. Jovanovič, J. Vavra, R. Buonsanti, N. Hodnik, Stability and degradation mechanisms of copper-based catalysts for electrochemical CO_2 reduction, Angewandte Chemie Int. Ed. 59 (35) (2020) 14736–14746.
[84] T. Takashima, K. Hashimoto, R. Nakamura, Mechanisms of PH-dependent activity for water oxidation to molecular oxygen by MnO_2 electrocatalysts, J. Am. Chem. Soc. 134 (3) (2012) 1519–1527.
[85] G. Chen, Y. Ling, Q. Li, H. Zheng, J. Qi, K. Li, J. Chen, J. Peng, L. Gao, M. Omran, F. He, Investigation on microwave carbothermal reduction behavior of low-grade pyrolusite, J. Mater. Res. Technol. 9 (4) (2020) 7862–7869.